eman ta zabal zazu
Universidad del País Vasco
Euskal Herriko Unibertsitatea

ZIENTZIA ETA TEKNOLOGIA FAKULTATEA
FACULTAD DE CIENCIA Y TECNOLOGÍA

Gradu Amaierako Lana / Trabajo Fin de Grado
Fisikako Gradua / Grado en Física

Quantum interference effects due to spin fields in mesoscopic rings

Egilea / Autor/a:
Alberto Hijano Mendizabal

Zuzendaria / Director/a:
Dario Bercioux
Asier Eiguren

Leioa, 2019ko ekainaren 20a / Leioa, 20 de junio de 2019

Acknowledgements

First, I would like to thank my supervisor Dario Bercioux for his outstanding work at directing this end-of-degree project. I am especially thankful for his advice involving this work, and for the time and commitment that he has devoted to this dissertation. I am also grateful to Asier Eiguren for agreeing to direct the project.

I would also like to thank Diego Frustaglia and José Pablo Baltanás for receiving Dario and me at the Universidad de Sevilla and sharing their comments on the obtained results.

I must also express my gratitude to my family for their support through the process of researching and writing this dissertation. I am specially grateful to my father for introducing me into the world of math and science.

Finally, I wish to thank the professors of the Double Degree in Physics and Electronic Engineering for their excellence in teaching. I wish to make a special mention to Raúl Pérez for being so passionate about his work and organizing the Physics Olympiad of the Basque Country.

Contents

1 Introduction

In this work we study the problem of quantum interference effects in mesoscopic rings due to spin fields. This system is interesting because of the multiple experiments carried out in semiconductor heterostructures and topological insulators. The work addresses physical effects that are fascinating both from a fundamental and applied point of view.

The thesis is organized with the following structure. Chapter 2 serves as a theoretical basis for the different quantum interference effects. We specifically consider the Aharonov-Bohm [2] and Aharonov-Casher [4] effects. In Chap. 3 we introduce the topological phases addressing the quantum interference effects. In the first part of the chapter, we define the Berry phase. S. Pancharatnam anticipated the existence of geometric phases, [11] but it was not until a paper written by Berry in 1984 that the systematic study of geometric phases began. [1] In the second part of the chapter we explain the Aharonov-Anandan (A-A) geometric phase, a generalisation of Berry phase. Finally, we calculate the A-A phase for a simple system, and show that it is equal to the Berry phase in the adiabatic approximation.

In Chap. 4 we describe the experiments carried out in a InAlAs/InGaAs heterostructure that study the oscillations of the electrical resistance due to the Al'tshuler-Aronov-Spivak (AAS) effect, [17] and the experimental evidence on the manipulation of an electron spin through a purely geometric effect. [19] These experiments are the main motivation of this work.

In Chap. 5 the basic definitions and properties of quantum graphs are introduced. Quantum graph theory is applied in Chap. 6 to solve quantum graph networks. In Chap. 7 we calculate the conductance of a 1D mesoscopic ring pierced by a magnetic flux and subject to Rashba spin-orbit coupling, based on the methods described in previous chapters.

Chapter 8 introduces an innovative method to study quantum networks under Rashba SO coupling and an inplane Zeeman field. The available states of an electron are studied and a spin evolution matrix $\hat{\boldsymbol{\mathcal{R}}}$ is defined. In Chap. 9, the method introduced in the previous chapter is used to study the conductance of polygons with RSO interaction and Zeeman field.

2 Interference types

Let a system be in a stationary state. If the environment, and hence the Hamiltonian $\hat{H}$, is slowly altered, it follows from the adiabatic theorem that at any instant the system will be in an instantaneous eigenstate of $\hat{H}$. If the Hamiltonian is returned to its original form, then, the system will return to its original state, apart from a phase factor. [1]

This phase factor is observable by quantum interference if the cycled system is recombined with another system whose Hamiltonian was kept constant.

2.1 Aharonov-Bohm effect

Consider a closed path that encircles a flux line. The magnetic field is zero in the circuit. The magnetic vector potential, on the contrary, has a finite value. In fact, the circulation of the vector potential is equal to the flux encircled by the circuit. The effect of such vector potential can be

interpreted as a geometrical phase change, also known as Berry phase.

$$\hat{H}_{\mathrm{AB}} = \frac{1}{2m}(\vec{p} + e\vec{A})^2 \tag{1}$$

Aharonov & Bohm studied this quantum phenomenon.[2] The Hamiltonian of this system is described by Eq. (1), where $\vec{p}$ is the momentum operator, e the charge of the electron and $\vec{A}$ the vector potential. What is surprising about the Aharonov-Bohm (AB) effect is the fact that classically, the vector potential is not associated to any physical effect, while the magnetic field is responsible for the classical magnetic force and it is the only physical quantity.[3]

The wave function of a particle in the presence of a vector potential $\vec{A}$ can be written as follows,

$$\Psi(r) = \exp\left(-\mathrm{i}\frac{2\pi}{\Phi_0}\int_0^r \vec{A}(\vec{r}\,') \cdot d\vec{r}\,'\right) \mathrm{e}^{\mathrm{i}kr}\Psi(0)\ . \tag{2}$$

The first term in Eq. (2) corresponds to the geometrical phase factor. The phase is proportional to the path integral of the vector potential. The second term is the dynamical phase factor. It is equal to the phase acquired by a free particle moving at wave-number k.

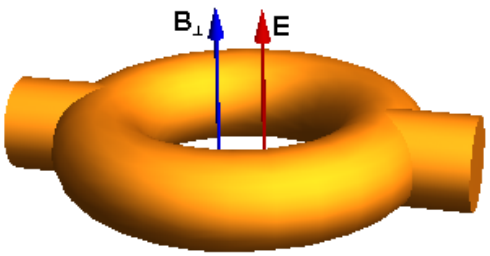

Figure 1: Mesoscopic ring pierced by a magnetic flux and a perpendicular electrical field.

Let a ring be pierced by a magnetic flux. Then, the phase acquired by a particle moving through the upper and lower paths will have the same magnitude, but opposite sign. Adding the contributions of all the possible paths will result in an interference effect. For certain values of the flux, there will be a destructive interference, and the transmission coefficient will be equal to zero.

2.2 Aharonov-Casher effect

The Aharonov-Casher (AC) effect is a quantum mechanical phenomenon suffered by spins travelling through an electric field.[4] It is the counterpart of the Aharonov-Bohm effect, where instead of having an electric charge moving in a magnetic field, we have a magnetic dipole moving through an electric field.

The effect was originally proposed for muons, but never observed so far. It can be observed in other systems where a coupling between the electron spin and an external electric field is obtained via spin-orbit coupling.

Rashba spin-orbit (RSO) coupling gives rise to intrinsic zero-field spin splitting in semiconductor heterostructures.[5] The motion of an electron in a two-dimensional electron gas (2DEG) through a perpendicular electric field, results in a magnetic field in the rest frame of the electron, that couples to the spin, of the particle as

$$\hat{H}_{\mathrm{SO}} = \frac{\hbar k_{\mathrm{SO}}}{m}(\vec{p} \times \hat{z}) \cdot \vec{\sigma} \,, \tag{3}$$

where $\vec{\sigma}$ is the Pauli vector and k_{SO} is the SO coupling strength. The SO coupling strength k_{SO} is related to the spin precession length L_{SO} by $\mathrm{L}_{\mathrm{SO}} = \pi/k_{\mathrm{SO}}$.[6;7]

Electrons have spin 1/2, which obeys SU(2) algebra.[8] Electrons acquire a SU(1) phase in the Aharonov-Bohm effect, which is to say that the wave function is multiplied by a complex phase. In the Aharonov-Casher effect, electrons acquire a SU(2) phase. The eigenfunctions in a 1D ring of radius R subject to RSO coupling read as follows.

$$\Psi^{\uparrow}_{+,n} = \exp(\mathrm{i}n\varphi) \begin{bmatrix} \sin\gamma/2 \\ \cos\gamma/2\mathrm{e}^{\mathrm{i}\varphi} \end{bmatrix} \,, \tag{4a}$$

$$\Psi^{\downarrow}_{+,n} = \exp(\mathrm{i}n\varphi) \begin{bmatrix} \cos\gamma/2 \\ -\sin\gamma/2\mathrm{e}^{\mathrm{i}\varphi} \end{bmatrix} \,, \tag{4b}$$

$$\Psi^{\uparrow}_{-,n} = \exp(-\mathrm{i}n\varphi) \begin{bmatrix} \cos\gamma/2 \\ -\sin\gamma/2\mathrm{e}^{\mathrm{i}\varphi} \end{bmatrix} \,, \tag{4c}$$

$$\Psi^{\downarrow}_{-,n} = \exp(-\mathrm{i}n\varphi) \begin{bmatrix} \sin\gamma/2 \\ \cos\gamma/2\mathrm{e}^{\mathrm{i}\varphi} \end{bmatrix} \,, \tag{4d}$$

where $\tan\gamma = 2k_{\mathrm{SO}}\mathrm{R}$. Here, the spin components depend on the travel direction, the orbital quantum number n and the spin state. Adiabaticity can not be obtained in systems with a finite Rashba SO term. Only in the strong SO coupling constant limit does the spin align with the local magnetic field.[9]

3 Topological phases

In the previous section we have studied the Aharonov-Bohm and its electromagnetic dual, the Aharonov-Casher effect. We have seen that a phase is associated to both effects, which can be observed by the interference of a cyclically varying system with another that was kept constant. Geometric phase factors are signatures of quantum motion. The adjective "geometric" emphasizes that such phase factors depend only in the closed path the quantum mechanical state forms in the projective Hilbert space. In particular, geometric phases are independent of parametrization of the path in the projective Hilbert space, which is to say that they are independent of the speed at which it has been traversed.[10]

Pancharatnam anticipated the quantal geometric phases in nonquantal polarization of light.[11] He studied the phase change acquired by polarized light when undergoing a sequence of polarizers such that its final polarization was the same as the initial polarization.

The intensity of the superposition of two polarized states of two beams of light with the same momenta is proportional to the inner product of the superposition:

$$I \propto (\langle A| + \langle B|)(|A\rangle + |B\rangle) = 2 + 2|\langle A|B\rangle| \cos(\mathrm{ph}\langle A|B\rangle) \; . \tag{5}$$

Two states are in phase when $\mathrm{ph}\langle A|B\rangle = 0$. The phase difference between two orthogonal states is not defined since their inner product $\langle A|B\rangle = 0$.

In his experiment, Pancharatnam changed the polarization from $|A\rangle$ to $|B\rangle$ to $|C\rangle$ and back to a state $|A'\rangle$ of the initial polarization. Pancharatnam identified the phase difference between the initial and final states as $\mathrm{ph}\langle A|A'\rangle$. He showed that this phase is equal to half the solid angle the geodesic triangle ABC forms in the Poincaré sphere.

3.1 Berry geometric phase

It was not until M. V. Berry published a seminal paper on the quantum-mechanical adiabatic theorem that geometric phases were explored in depth, both from a theoretical and applied approach. Berry, who was unaware of Pancharatnam's work, deduced the general formula for systems whose Hamiltonian changed by varying parameters $\boldsymbol{R} = (X, Y, ...)$. The system evolved round a closed path C in parameter space between times $t = 0$ and $t = T$, such that $\boldsymbol{R}(T) = \boldsymbol{R}(0)$. He required that the time T should be large for the adiabatic approximation to apply.[1]

At any instant, the system will be in an instantaneous eigenstate of $\hat{H}(\boldsymbol{R})$

$$\hat{H}(\boldsymbol{R})|n(\boldsymbol{R})\rangle = E_n(\boldsymbol{R})|n(\boldsymbol{R})\rangle \; . \tag{6}$$

Adiabatically, a system prepared in a state $|n(\boldsymbol{R}(0))\rangle$ will evolve as

$$|\psi(t)\rangle = \mathrm{e}^{\frac{-\mathrm{i}}{\hbar}\int_0^t dt' E_n(\boldsymbol{R}(t'))} \mathrm{e}^{\mathrm{i}\gamma_n(t)} |n(\boldsymbol{R}(t))\rangle \; . \tag{7}$$

The first exponential in (7) is the usual dynamical phase factor. The second term, $\gamma_n(t)$ is non-integrable; it can not be written as a function of $\boldsymbol{R}$ and is not single-valued $\gamma_n(T) \neq \gamma_n(0)$. The state in (7) must satisfy the time dependent Schrödinger equation, so that

$$\dot{\gamma}_n(t) = \mathrm{i}\langle n(\boldsymbol{R}(t))|\nabla_{\boldsymbol{R}} n(\boldsymbol{R}(t))\rangle \cdot \dot{\boldsymbol{R}}(t) \; . \tag{8}$$

The geometrical phase change, or the Barry phase as it is now known, round a circuit C is given by

$$\gamma_n(C) = \mathrm{i} \oint_C \langle n(\boldsymbol{R})|\nabla_{\boldsymbol{R}} n(\boldsymbol{R})\rangle \cdot d\boldsymbol{R} \; . \tag{9}$$

The normalization of $|n(\boldsymbol{R})\rangle$ guarantees that $\langle n(\boldsymbol{R})|\nabla_{\boldsymbol{R}} n(\boldsymbol{R})\rangle$ is purely imaginary, so that γ_n is real.

Three-dimensional parameter spaces are of special interest, for example, the Hamiltonian could depend on a time varying magnetic field $\vec{B}$. In such cases, Stokes theorem can be applied to (9). Berry phase is then given by a surface integral in parameter space bounded by C:

$$\begin{aligned}\gamma_n(C) =& \mathrm{i}\iint_{S(C)} d\boldsymbol{S}\cdot\nabla\times\langle n|\nabla n\rangle \\ =& \mathrm{i}\iint_{S(C)} d\boldsymbol{S}\cdot\sum_{m\neq n}\langle\nabla n|m\rangle\times\langle m|\nabla n\rangle\ .\end{aligned} \tag{10}$$

The term $\langle m|\nabla n\rangle$ can be obtained from (6) as

$$\langle m|\nabla n\rangle = \langle m|\nabla\hat{H}|n\rangle/(E_n - E_m),\ m\neq n\ . \tag{11}$$

Thus, the Berry phase of a system associated to an adiabatic process described by a closed path in a three dimensional parameter space is given by

$$\gamma_n(C) = -\iint_{S(C)} \boldsymbol{V}_n(\boldsymbol{R})\cdot d\boldsymbol{S}\ , \tag{12}$$

where $\boldsymbol{V}_n$ is the Berry curvature

$$\boldsymbol{V}_n(\boldsymbol{R}) = \mathrm{Im}\sum_{m\neq n}\frac{\langle n(\boldsymbol{R})|\nabla\hat{H}(\boldsymbol{R})|m(\boldsymbol{R})\rangle\times\langle m(\boldsymbol{R})|\nabla\hat{H}(\boldsymbol{R})|n(\boldsymbol{R})\rangle}{(E_m(\boldsymbol{R}) - E_n(\boldsymbol{R}))^2}\ . \tag{13}$$

$\boldsymbol{V}_n$ is analogous to a magnetic field whose vector potential is $\langle n|\nabla n\rangle$.

In reference to the last paragraph, the Aharonov-Bohm phase can be seen as a special case of geometric phase. Consider a magnetic field consisting on a single flux line with flux Φ. Let a charged particle be confined to a box situated at $\vec{R}$ (the position of the box will be the varying parameter of the Hamiltonian). The states of the system satisfy

$$\hat{H}(\vec{p} - q\vec{A}(\vec{R}), \vec{r} - \vec{R})|n(\vec{R})\rangle = E_n|n(\vec{R})\rangle\ . \tag{14}$$

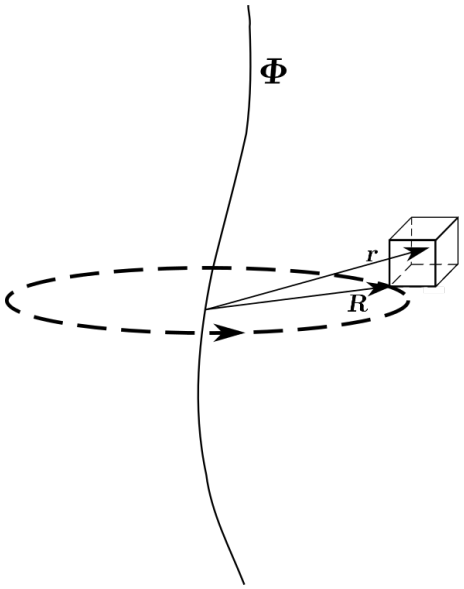

Figure 2: Charged particle confined to a box travelling round a flux line.

The eigenstates of the system have the following form

$$\langle \vec{r}|n(\vec{R})\rangle = \mathrm{e}^{\mathrm{i}\frac{q}{\hbar}\int_{\vec{R}}^{\vec{r}} d\vec{r}'\cdot\vec{A}(\vec{r}')}\psi_n(\vec{r}-\vec{R})\ , \tag{15}$$

where $\psi_n(\vec{r}-\vec{R})$ are the eigenstates of the flux free system. If the box is transported round the flux line on a circuit C, it can be shown that the geometrical phase will be given by

$$\gamma_n = \frac{q}{\hbar}\oint_C \vec{A}(\vec{R})\cdot d\vec{R} = \frac{q}{\hbar}\Phi\ . \tag{16}$$

Equation (16) shows that γ_n is independent of n and C. We have proven that the AB phase is a particular case of the geometric phase in the adiabatical regime. Following an analogous procedure, it can be shown that the AC phase is also a particular case of geometric phase.[12]

3.2 Aharonov-Anandan geometric phase

Y. Aharonov and J. Anandan generalised Berry's work by proving the existence of a phase associated with all cyclic evolutions. This phase is universal in the sense that it is the same for all motions along the curves of the Hilbert space $\mathcal{H}$ which project to the same closed curve $\hat{C}$ in the projective Hilbert space $\mathcal{P}$ of rays of $\mathcal{H}$ and all Hamiltonians. In the adiabatic limit, this phase tends to the Berry phase.[13]

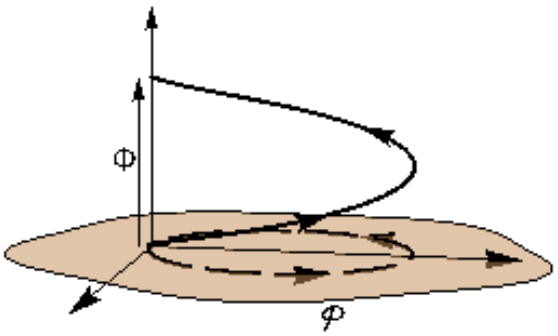

Figure 3: A cyclic evolution projected into the projective Hilbert space $\mathcal{P}$.

Let a state $|\psi(t)\rangle$ evolve according to the Schrödinger equation

$$\hat{H}(t)|\psi(t)\rangle = \mathrm{i}\hbar\frac{d}{dt}|\psi(t)\rangle \tag{17}$$

so that the system returns to the initial state apart from a phase factor at time $t = \tau$, $|\psi(\tau)\rangle = \mathrm{e}^{\mathrm{i}\phi}|\psi(0)\rangle$. Let $\Pi : \mathcal{H} \to \mathcal{P}$ be the projection map defined by $\Pi(|\psi\rangle) = \{|\psi'\rangle : |\psi'\rangle = c|\psi\rangle, c \in \mathbb{C}\}$. Then, the projection the curve C defines in $\mathcal{H}$, $\hat{C} \equiv \Pi(C)$, is a closed curve in $\mathcal{P}$.

We now define $|\tilde{\psi}(t)\rangle = \mathrm{e}^{-\mathrm{i}f(t)}|\psi(t)\rangle$ such that $f(\tau) - f(0) = \phi$. Then, $|\tilde{\psi}(\tau)\rangle = |\tilde{\psi}(0)\rangle$, and from (17),

$$-\frac{df}{dt} = \frac{1}{\hbar}\langle\psi(t)|\hat{H}|\psi(t)\rangle - \langle\tilde{\psi}(t)|\mathrm{i}\frac{d}{dt}|\tilde{\psi}(t)\rangle \ . \tag{18}$$

Integrating (18) from $t = 0$ to $t = \tau$,

$$\phi_g \equiv \phi + \frac{1}{\hbar}\int_0^\tau \langle\psi(t)|\hat{H}|\psi(t)\rangle dt \ , \tag{19}$$

where

$$\phi_g = \int_0^\tau \langle\tilde{\psi}(t)|\mathrm{i}\frac{d}{dt}|\tilde{\psi}(t)\rangle dt \tag{20}$$

is the Aharonov-Anandan phase. Equation (20) explains that ϕ_g is the contribution to the phase ϕ excluding the dynamical phase ϕ_d. Note that adiabaticity is not a requirement to define ϕ_g. Further, the Hamiltonian need not be cyclic $\hat{H}(\tau) \neq \hat{H}(0)$. In fact, ϕ_g is independent of ϕ and $\hat{H}$ for a given closed curve $\hat{C}$.

Furthermore, ϕ_g is independent of t, and it is determined up to $2\pi n$, $n \in \mathbb{N}$.

Consider now a slowly varying $\hat{H}(t)$. If we write the state of the system as

$$|\psi(t)\rangle = \sum_n c_n(t)\mathrm{e}^{-\frac{\mathrm{i}}{\hbar}\int E_n(t)dt}|n(t)\rangle \ , \tag{21}$$

it follows from Eq. (17) that

$$\dot{c}_m = -c_m\langle m|\dot{m}\rangle - \sum_{n\neq m} c_n \frac{\langle m|\dot{H}|n\rangle}{E_n - E_m} \mathrm{e}^{\frac{\mathrm{i}}{\hbar}\int (E_m - E_n)dt} \ . \tag{22}$$

If the system is in an eigenstate at $t = 0$, $c_n(0) = \delta_{nm}$, and the condition for adiabaticity

$$\sum_{n\neq m} \left| \frac{\hbar\langle m|\dot{H}|n\rangle}{(E_m - E_n)^2} \right| \ll 1 \tag{23}$$

is satisfied, the last term in Eq. (22) is negligible and the system would therefore continue as an eigenstate of $\hat{H}(t)$, and

$$c_n(t) \simeq \mathrm{e}^{-\int \langle n|\dot{n}\rangle dt} c_n(0) \ . \tag{24}$$

In this approximation, we recover the Berry phase given by (9), where the varying parameter is t.

The Berry phase can be seen as a geometrical property of the parameter space defining Hamiltonian $\hat{H}$. On the contrary, the Aharonov-Anandan phase can be associated with a closed curve in the projective Hilbert space $\mathcal{P}$.

3.3 Example: Spin-$\frac{1}{2}$ particle in a magnetic field

At the beginning of this section we discussed how Pancharatnam showed that the phase acquired by light when undergoing a cyclic change of polarization is equal to half the solid angle the polarization evolution forms in the Poincaré sphere. Berry showed that the geometrical phase factor for a spin interacting with a slowly varying magnetic field $\vec{B}$ round a circuit C via the Hamiltonian

$$\hat{H} = \mu\vec{B}\cdot\vec{\sigma} \tag{25}$$

in a spin state $-s \leq n \leq s$, is

$$\mathrm{e}^{\mathrm{i}\gamma_n(C)} = \mathrm{e}^{-\mathrm{i}n\Omega(C)} \ , \tag{26}$$

where Ω is the solid angle that C subtends at $\vec{B} = 0$ in the parameter space.[1] Particularly, for spin $\frac{1}{2}$ particles, $\gamma_n = \mp\frac{1}{2}\Omega$.

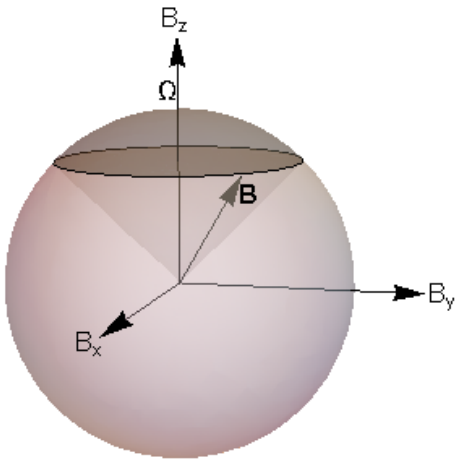

Figure 4: Evolution of a varying magnetic field in $\vec{B}$ parameter space.

This relation between polarizations and quantum states of spin-$\frac{1}{2}$ particles, that is, with two-state systems is unsurprising, because any polarization of light traveling in a fixed direction is a superposition of two basis polarizations. [14]

We now consider a spin-$\frac{1}{2}$ particle with a magnetic moment in a homogeneous magnetic field along the z axis $\vec{B} = B\hat{z}$. In this case the adiabatic approximation is not valid. The Hamiltonian of this system is given by

$$\hat{H} = \mu B \begin{pmatrix} 1 & 0 \\ 0 & -1 \end{pmatrix} , \tag{27}$$

where the states evolve as

$$|\psi(t)\rangle = \mathrm{e}^{-\mathrm{i}\mu B t \sigma_z/\hbar} |\psi(0)\rangle . \tag{28}$$

Let the initial spin state lie on the xz plane, so that the spin forms an angle θ with the z axis:

$$|\psi(0)\rangle = \begin{pmatrix} \cos(\theta/2) \\ \sin(\theta/2) \end{pmatrix} . \tag{29}$$

Applying Eq. (28) to (29),

$$|\psi(0)\rangle = \begin{pmatrix} \mathrm{e}^{-\mathrm{i}\mu B t/\hbar} \cos(\theta/2) \\ \mathrm{e}^{\mathrm{i}\mu B t/\hbar} \sin(\theta/2) \end{pmatrix} , \tag{30}$$

which corresponds to the spin direction precessing around the $-z$ axis with an angular velocity $\omega = 2\mu B t/\hbar$. The evolution is periodic with period $\tau = \pi\hbar/\mu B$. The total phase acquired during a period is $\phi = \pi$, $|\psi(\tau)\rangle = -|\psi(0)\rangle$. Using Eq. (19), we obtain the geometric phase

$$\phi_g = \pi(1 + \cos\theta) . \tag{31}$$

The geometric phase in (31) is equal to half the solid angle subtended by the spin state in the Bloch sphere.

Recalling the result obtained for the Berry phase in a spin in a slowly varying magnetic field $\vec{B}'$, the geometric phase was equal to half the solid angle subtended by the curve traced by the magnetic field in parameter space. The magnetic field must vary slowly enough so that the adiabatic approximation is valid and the system is in an eigenstate at every time.

We discussed in this section that the geometric phase is independent of the Hamiltonian as long as the closed curve in the projective Hilbert space is the same. The spin state will also move through the same $\hat{C}$ for a $\vec{B}' = (B_r \cos\omega t, -B_r \sin\omega t, B_z)$ with $\cot\theta = (B_z - B)/B_r$, where $B_r \neq 0$. In the adiabatic regime, $\omega \ll \mu B'/\hbar$ so that $\cot\theta = B_z/B_r$. In this limit the spin is aligned with the magnetic field, so the curve traced by $\vec{B}'$ in parameter space will be $\Omega = 2\pi(1 + \cos\theta)$. Therefore we recover the Berry phase in the adiabatical limit.

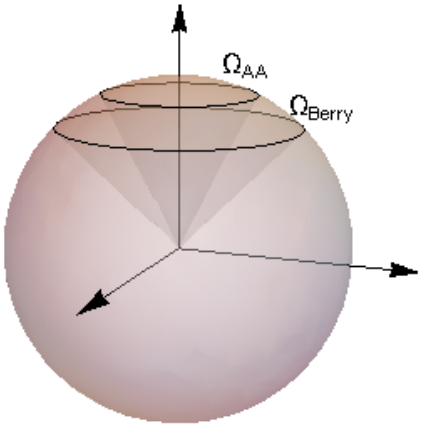

Figure 5: Graphical representation of the solid angle that give rise to the Berry phase and the AA phase.

4 Experimental data

Interference effects under the presence of Rashba SO coupling have been studied in multiple experiments. [15;16] Nagasawa *et al.* realised a two dimensional electron gas in a InAlAs/InGaAs heterostructure and studied the oscillations of the electrical resistance as a function of the back gate and a magnetic flux. [17] They concluded that the geometric phase of electron spin shifts the electrical resistance towards weaker spin-orbit interaction regions because of the Aharonov-Casher effect.

True adiabaticity cannot be achieved in systems subject to SO coupling. In this context, adiabaticity implies that an electron is moved slowly enough that the spin's magnetic moment

stays aligned with the local magnetic field. Adiabaticity is therefore favored by a strong spin-orbit interaction. The spin precesses around the radial in-plane effective magnetic field.

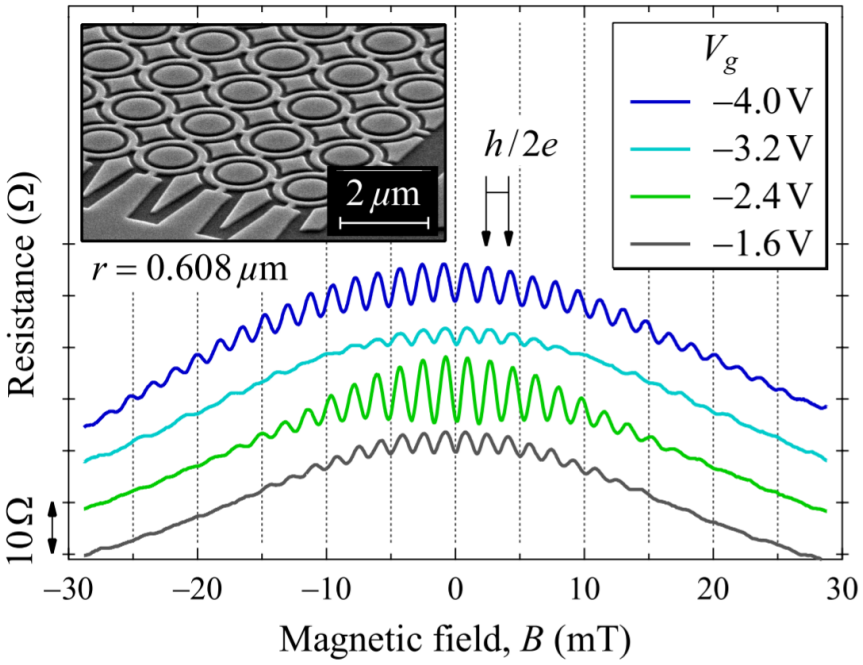

Figure 6: Magnetoresistance curves as a function of the applied magnetic field for different values of the gate voltage.[17]

Figure 6 shows the experimental results obtained in a 40x40 ring array with radius $r = 0.608\mu$m. All measurements were performed at a temperature of 1.7 K. The Rashba SO strength k_{SO} is controlled by the gate voltage V_{g}. The gate voltage also affects the electron wavelength. The curves are shifted vertically for clarity.

The AB effect predicts that the oscillations of the resistance have a period of a quantum flux $\Phi_0 = h/e$. However, the oscillations observed have a period of half a flux quantum $\Phi_0/2$. This is due to the Al'tshuler-Aronov-Spivak (AAS) effect, the AB effect in the time-reversal paths.[18] Averaging over a large number of rings allows the measurement of the AAS effect instead of the AB effect. One of the advantages of the AAS effect is that it is more robust with respect to noise. The AAS effect is also responsible for the damping of the amplitude of the resistance oscillations at higher magnetic fields.

In a later work, Nagasawa *et al.* reported about experimental evidence on the manipulation of an electron spin through a purely geometric effect in an InGaAs-based quantum ring beyond the adiabatic limit. While the relevance of the Berry phase has been demonstrated in a large variety of experiments, the geometric phase of an electron had not been observed directly and controlled independently from dynamical phases. They observed a phase shift of the Aharonov-Casher interference pattern towards the small spin-orbit-coupling regions by applying an in-plane magnetic field.[19]

The phase shift originates exclusively from the modulation of a pure geometric phase component of the electron, independently from dynamical phases. The dynamical phase is acquired by spins precessing around a magnetic field. In mesoscopic systems, spins acquire an additional geometric phase that depends on the path of the spin, which is proportional to the solid angle in the magnetic-field space. In Fig. 7e, a parallel magnetic field is applied to a Rashba ring. The total magnetic field seen by the electron is uniformly tilted towards the applied field direction, which changes the solid angle in the magnetic-field space (Fig. 7f). This allows for controlled modulation of the pure geometric phase independently of the dynamical phase.

The dependence of the AC effect on the in-plane magnetic field $B_{\parallel}$ in experiment is shown in Fig. 8 (a,b). As $B_{\parallel}$ is applied, the amplitude of the AC effect is suppressed because of spin-induced time reversal symmetry breaking.

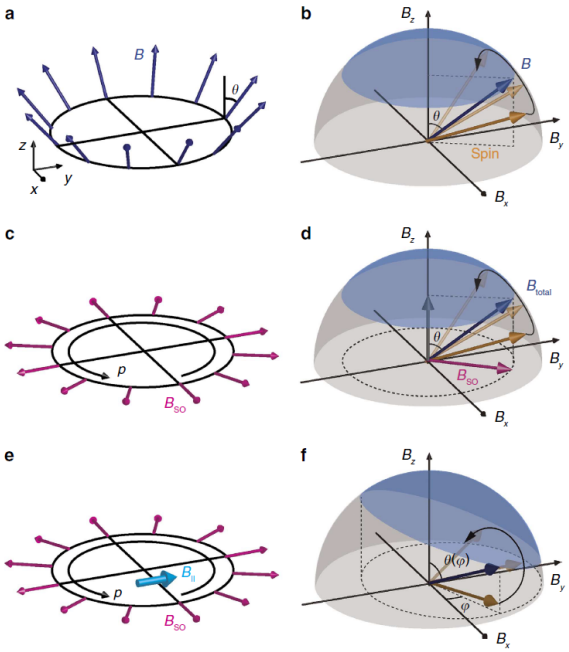

Figure 7: Textured magnetic field in a ring (a,c,e) and spin precession around $\vec{B}$ (b,d,f). The geometric phase is proportional to the solid angle subtended by the total effective magnetic field. [19]

Further, the AC oscillations exhibit a quadratic shift with $B_{\parallel}$ towards weaker Rashba SO-coupling strengths. The observed shift is explained by the sole modulation of the geometric phase as shown in Fig. 7f.

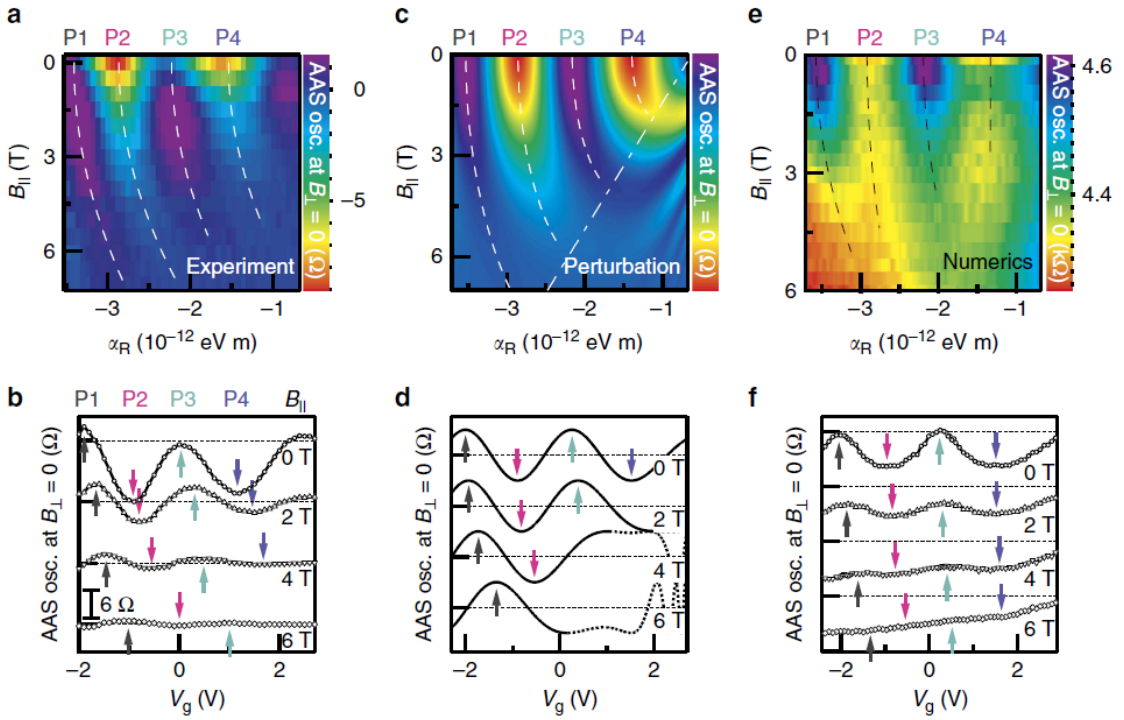

Figure 8: The AC oscillations are shown as a function of the Rashba SO-coupling constant α_R and the in-plane $B_\parallel$ field (a,c,e). The AC oscillations are shown for four different $B_\parallel$ as a function of the gate voltage, V_g. Panels (a,b) correspond to experimental data, (c,d) to perturbation theory for a 1D Rashba ring with a small $B_\parallel$ field and (e,f) to numerical calculations of the AC effect in disordered multimode rings.[19]

5 Quantum graphs

In order to investigate quantum transport in rings with magnetic field and SO coupling, we will use the technique of quantum graphs.

A metric graph is a mathematical structure that consists of a set of vertices and edges which connect the vertices. A graph can be graphically represented as a set of dots representing the vertices, joined by a set of bonds representing the edges. A quantum graph is a metric graph equipped with a self-adjoint second-order Laplacian operator $\hat{L}$.[20]

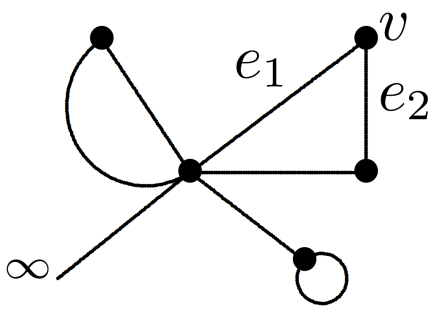

Figure 9: Graphical representation of a quantum graph. [25]

Graphs and quantum graphs have a variety of uses in multiple fields: electrical networks can be described as nodes joined by branches representing discrete devices, [21] the system of veins or brain graphs in the human body, [22] the continuity principle in fluid dynamics, abstract model of quantum chaos, quantum wires, photonic crystals and thin wave guidelines. [23]

5.1 Compact finite graphs

Compact finite graphs are a subset of metric graph which consist of a finite number of edges, each of finite length. [25] All vertices must be linked to at least another vertex. Multiple links between the same vertices are allowed, as well as loops.

5.2 Differential operator

An electron moving through a system is subject to a Hamiltonian. The Schrödinger operator can be defined on the metric graph for each edge:

$$\hat{H}_j = \frac{1}{2m}\left(-\mathrm{i}\hbar\frac{d}{dr} + a_j(r)\right)^2 + b_j(r)\ , \tag{32}$$

where $a_j(r)$ and $b_j(r)$ and are the magnetic and electric potential respectively.

5.3 Boundary conditions

We consider the set of functions $\mathcal{D}$ which are continuous and complex valued functions, $\Psi(x) \in \mathcal{D}$ with $\Psi(x) = \psi_j(x_j)$, $0 \leq x_j \leq l_j$ where l_j is the length of each edge. [24]

The functions $\psi_j(x_j)$ are piecewise continuous and have square integrable first derivatives. At each vertex two boundary conditions must be fulfilled. The most common conditions are the Dirichlet and Neumann boundary conditions: the continuity of $\Psi(x)$ at the vertices, and the current continuity:

$$\sum_j \psi_j'(\alpha) = 0\ , \tag{33}$$

where the sum runs over all edges that are connected to the vertex α. The derivative must be applied outward from a vertex, that is to say,

$$\psi_j'(\alpha) = \begin{cases} \psi_j'(0), \alpha \text{ is the left endpoint} \\ -\psi_j'(l_j), \alpha \text{ is the right endpoint .} \end{cases} \tag{34}$$

The concept of extended normal derivative must be introduced to apply the second boundary condition. The definition might vary depending on the differential operator, for a spinless particle the extended normal derivative can be expressed as

$$\boldsymbol{D}\psi_j(\alpha) \equiv \psi_j'(\alpha) := \begin{cases} \lim_{r\to\alpha}(\frac{d}{dr} + \mathrm{i}\frac{a_j}{\hbar})\psi_j, \alpha \text{ is the left endpoint} \\ \lim_{r\to\alpha} -(\frac{d}{dr} + \mathrm{i}\frac{a_j}{\hbar})\psi_j, \alpha \text{ is the right endpoint .} \end{cases} \tag{35}$$

Quantum graphs will be used in subsequent sections to solve the Schrödinger equation in different regions or wires of a quantum network. Imposing appropriate boundary conditions, the eigenstates of the system can be obtained.

6 Application of quantum graph theory: the case of polygonal closed structures

Solving the Schrödinger equation for a spinless particle constrained to a 1D ring is a simple task. A ring can be seen as a 1D crystal, where the periodicity of the crystal is equal to the perimeter of the ring. Periodic boundary conditions must be used to quantify the eigenvalues.

Adding Rashba SO coupling into the system can complicate the resolution of the problem since the direction of the momentum, and therefore the direction of the effective magnetic field, depends on the position. Another approach to find the eigenfunctions of the system can be considering a series of regular polygons of constant perimeter. In the limit of infinite number of vertices, the polygon converges to a single-channel circular conductor.[26] This method solves locally the issue of a directionally changing momentum. Input/output semi-infinite wires will be attached at opposite vertices in order to study the conductance of the ring.

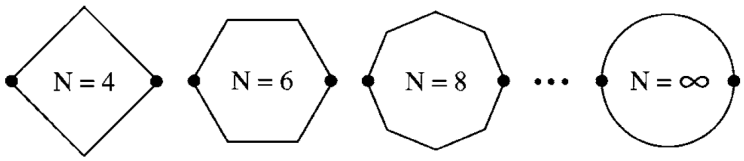

Figure 10: Series of regular polygons with constant perimeter P. The dots represent the vertices where input and output leads are attached.[26]

A polygon can be seen as a quantum network where all vertices are bond through edges to their two first neighbours. Therefore, quantum graphs can be used to approach the problem. The Schrödinger equation will be solved for each edge in subsections 6.1-6.4 for different Hamiltonians, and boundary conditions will be applied at 6.7.

The average momentum of incoming electrons must fulfill certain limits. To start with, the Fermi wavelength of the electron must be much smaller than the natural length of the system. Smaller

wave numbers are more prone to scattering and decoherence.[19;27] In our system, the requirement is that the wavelength of the electron must be much smaller than the perimeter of the polygon:

$$k \gg \frac{2\pi}{P} \, . \tag{36}$$

The wavelength will also be limited by the size of the sides of the polygon. On the one hand, the wavelength of the electron must be smaller than the length of the side of the polygon so that multiple wavelengths fit in one side. Otherwise, the electron would not "see" the side. On the other hand, in the specific case of the ring, the requirement is just the opposite, the wavelength must be much greater than the length of the side of the polygon, so that each side is hardly noticed by the electron and the polygon can really be treated as a ring:

$$k \ll \frac{2\pi N}{P} = \frac{2\pi}{L} \, , \tag{37}$$

where N is the number of sides of the polygon used to simulate the ring, and L is the length of each side. Obviously, the greater the number of sides, the more will the polygon resemble the results of the ring.

6.1 Magnetic flux

The solution of the Schrödinger equation for a potential free particle in a 1D wire of length l can be written as

$$\mathbf{\Psi} = \frac{1}{\sin(kl)} [\sin k(l-r)\mathbf{\Psi}_\alpha + \sin(kr)\mathbf{\Psi}_\beta] \, , \tag{38}$$

where $\mathbf{\Psi}_\alpha$ and $\mathbf{\Psi}_\beta$ are the values taken by the wave function at its endpoints and k is related to the energy as

$$\varepsilon = \frac{k^2\hbar^2}{2m} \, . \tag{39}$$

In order to obtain the wave function of the whole polygon, the continuity of probability current must be applied at the vertices.[1]

We consider an electron traveling through said polygon. If a magnetic flux is applied inside the polygon, a magnetic-vector potential $\vec{A}$ will arise. Let us assume that the magnetic flux is obtained by an homogeneous magnetic field inside a circumference of radius r_0 centered at the origin ($r_0 < \frac{l}{2\tan(\pi/N)}$). The magnetic vector potential can then be expressed as[28]

$$\vec{A} = \begin{cases} \frac{B_0 r}{2}, \text{if } r < r_0 \\ \frac{B_0 r_0^2}{2r} = \frac{\Phi}{2\pi r}, \text{if } r > r_0 \, . \end{cases} \tag{40}$$

In Eq. (40), B_0 expresses the value of the magnetic field piercing the polygon, whereas $\Phi = B_0\pi r^2$ is the value of the magnetic flux. The Hamiltonian for an electron in the presence of a magnetic vector potential can be written as

$$\hat{H} = \frac{1}{2m}(\vec{p} + e\vec{A})^2 + V(\vec{r}, \vec{p} + e\vec{A}) \, , \tag{41}$$

[1] The continuity of the wave function is satisfied by the use of $\mathbf{\Psi}_\alpha$ and $\mathbf{\Psi}_\beta$

where e is the magnitude of the charge of the electron. The wave function of the wire corresponding to this new Hamiltonian can be expressed as [30]

$$\mathbf{\Psi}_{\alpha\beta} = \mathrm{e}^{-\mathrm{i}f(r)}\mathbf{\Psi}_0 \ , \tag{42}$$

where $\mathbf{\Psi}_0$ is equal to the flux free Hamiltonian solution with energy ε_0 and

$$f(r) = \frac{e}{\hbar}\int_\alpha^r d\vec{r}\,' \cdot \vec{A}(\vec{r}\,') \ , \tag{43}$$

that is to say, $f(r)$ is proportional to the vector line integral of the magnetic vector potential. $f(\beta) = \frac{e}{\hbar}\frac{\Phi}{N} = \frac{2\pi}{N}\frac{\Phi}{\Phi_0}$, since the circulation of the magnetic vector potential through the polygon is equal to the magnetic flux and the line integral over each edge is the same.

Applying the Hamiltonian to (42), the energy of the wave function is found to be the same as the magnetic flux free energy ε_0.

6.2 Rashba spin-orbit coupling

Let the Hamiltonian for a system subject to Rashba SO coupling be written as

$$\hat{H} = \hat{H}_0 + \hat{H}_{\mathrm{SO}} \ , \tag{44}$$

where $\hat{H}_0 = \frac{\vec{p}^2}{2m} + V(\vec{r})$ is a Rashba coupling free Hamiltonian and $\hat{H}_{\mathrm{SO}}$ is given by Eq. (3). The 1D Hamiltonian operator must be derived with care, different Hamiltonians have been used by different authors. The procedure to obtain the correct 1D Hamiltonian operator for electrons moving on a ring in the presence of Rashba SO interaction was derived by Meijer *et al.* They show that the terms proportional to derivatives with respect to r can not be discarded. [29] Equation (3) in cylindrical coordinates can be written as

$$\hat{H}_{\mathrm{SO}} = \frac{\hbar k_{\mathrm{SO}}}{m}(\vec{p}\times\hat{z})\cdot\vec{\sigma} = \frac{\hbar^2 k_{\mathrm{SO}}}{m}\left(\mathrm{i}\sigma_\varphi\frac{\partial}{\partial r} - \mathrm{i}\sigma_r\frac{1}{r}\frac{\partial}{\partial\varphi}\right) \ . \tag{45}$$

The term $\mathrm{i}\sigma_r\frac{1}{R}\frac{\partial}{\partial\varphi}$ is not Hermitean with respect to the standard inner product. The correct 1D Hamiltonian is given by

$$\hat{H}_{\mathrm{SO}} = \frac{\hbar^2 k_{\mathrm{SO}}}{m}\left(-\mathrm{i}\frac{1}{2R}\sigma_\varphi - \mathrm{i}\sigma_r\frac{1}{R}\frac{\partial}{\partial\varphi}\right) \ . \tag{46}$$

Using the quantum graph approach removes the mentioned problem, since the wires have no local curvature.

Let $\{\varepsilon_0\}$ and $\{\psi_0\}$ be the set of eigenvalues and eigenfunctions of $\hat{H}_0$ respectively. If $[H_{\mathrm{SO}}, V] = 0$, the eigenfunctions of (44) for a wire can be written as

$$\mathbf{\Psi}_{\alpha\beta} = \mathrm{e}^{-\mathrm{i}(\hat{\gamma}_{\alpha\beta}\times\hat{z})\cdot\vec{\sigma}k_{\mathrm{SO}}r}\mathbf{\Psi}_0 \ , \tag{47}$$

where $\hat{\gamma}_{\alpha\beta}$ is the unitary vector pointing along the wire from α to β. The Pauli vector is present in the exponential, so it is in fact a SU(2) phase. The energy associated to said eigenfunction is

$$\varepsilon = \varepsilon_0 - \frac{\hbar^2 k_{\mathrm{SO}}^2}{2m} \ . \tag{48}$$

6.3 Magnetic flux+spin-orbit coupling

Let us now consider an electron confined to a regular polygon with both a magnetic potential and a SO coupling.

$$\hat{H} = \frac{1}{2m}(\vec{p} + e\vec{A})^2 + \frac{\hbar k_{\mathrm{SO}}}{m}((\vec{p} + e\vec{A}) \times \hat{z}) \cdot \vec{\sigma} \, . \tag{49}$$

Taking Eqs. (38), (42) and (47) into account, we obtain that the the eigenfuntions and eigenvalues of (49) for each edge are

$$\mathbf{\Psi} = \frac{\mathrm{e}^{-\mathrm{i}f(r)}\mathrm{e}^{-\mathrm{i}(\hat{\gamma}_{\alpha\beta}\times\hat{z})\cdot\vec{\sigma}k_{\mathrm{SO}}r}}{\sin(kl)}[\sin k(l-r)\mathbf{\Psi}_\alpha + \sin(kr)\mathrm{e}^{\mathrm{i}f(l)}\mathrm{e}^{\mathrm{i}(\hat{\gamma}_{\alpha\beta}\times\hat{z})\cdot\vec{\sigma}k_{\mathrm{SO}}l}\mathbf{\Psi}_\beta] \, , \tag{50}$$

$$\varepsilon = \frac{\hbar^2(k^2 - k_{\mathrm{SO}}^2)}{2m} \, . \tag{51}$$

The results of previous sections can be used to rearrange the wave function as seen in Eq. (50). The first term corresponds to the phase acquired by the AB effect, while the second term arises due to the AC effect. It should be noted that k in Eqs. (50-51) does not represent the wavenumber of a free particle, but rather a relation between the wavenumber and k_{SO}. It is a well known fact that the quantum wire dispersions $\varepsilon(k)$ in the presence of Rashba SO interaction shift horizontally as seen in Fig. (13). The energy spectrum is given by Eq. (101), where the k corresponds to the plane wave factor of states at the same Fermi energy.

6.4 Input/output leads

Let the polygons be coupled to two 1D leads without SO coupling at opposite vertices. If an electron is injected with wavenumber k and spin $\sigma = \pm$, with corresponding spinor $\boldsymbol{\chi}_\sigma$, the wave function alongside the input and output leads can be written as

$$\mathbf{\Psi}_{\mathrm{in}}(r) = \mathrm{e}^{\mathrm{i}kr}\boldsymbol{\chi}_\sigma + \sum_{\sigma'} r_{\sigma'\sigma}\mathrm{e}^{-\mathrm{i}kr}\boldsymbol{\chi}_{\sigma'}, \tag{52}$$

$$\mathbf{\Psi}_{\mathrm{out}}(r) = \sum_{\sigma'} t_{\sigma'\sigma}\mathrm{e}^{\mathrm{i}kr}\boldsymbol{\chi}_{\sigma'}. \tag{53}$$

The eigenstates are a combination of complex exponentials. Here $r_{\sigma'\sigma}$ and $t_{\sigma'\sigma}$ are the spin-resolved reflection and transmission coefficients respectively. They depend on the spin state of the incoming wave function, as well as the state of the reflected or transmitted state.

6.5 Probability density and probability current

The wave function of the polygon is obtained by imposing the continuity of the probability current at the nodes.[7] The continuity equation relates the probability density ρ with the probability current, $\vec{j}$:

$$\frac{\partial\rho}{\partial t} + \nabla \cdot \vec{j} = 0 \, . \tag{54}$$

The probability density is given by the square of the modulus of the wave function:

$$\rho = |\Psi|^2 = \Psi^*\Psi \, . \tag{55}$$

Differentiating (55) with respect to t,

$$\frac{\partial \rho}{\partial t} = \frac{\partial \Psi^*}{\partial t}\Psi + \Psi^* \frac{\partial \Psi}{\partial t} \ . \tag{56}$$

Using the Schrödinger equation and its complex conjugate, $\hat{H}^*\Psi^* = -\mathrm{i}\hbar\frac{\partial \Psi^*}{\partial t}$,[31] (56) becomes

$$\frac{\partial \rho}{\partial t} = -\frac{1}{\mathrm{i}\hbar}[(\hat{H}^*\Psi^*)\Psi - \Psi^*(\hat{H}\Psi)]. \tag{57}$$

Substituting (49) into (57) we get that

$$\frac{\partial \rho}{\partial t} = \frac{\mathrm{i}\hbar}{2m}\nabla \cdot [\Psi^*\nabla\Psi - \nabla\Psi^*\Psi + 2\mathrm{i}\frac{e}{\hbar}\vec{A}\Psi^*\Psi + 2\mathrm{i}k_{\mathrm{SO}}\Psi^*(\hat{z}\times\vec{\sigma})\Psi] \ , \tag{58}$$

and applying (58) to (54),

$$\vec{\jmath} = \frac{-\mathrm{i}\hbar}{2m}[\Psi^*\nabla\Psi - \nabla\Psi^*\Psi + 2\mathrm{i}\frac{e}{\hbar}\vec{A}\Psi^*\Psi + 2\mathrm{i}k_{\mathrm{SO}}\Psi^*(\hat{z}\times\vec{\sigma})\Psi] \ . \tag{59}$$

The SO interaction term in the Schrödinger equation places an additional spin-dependent term in the probability current density.[32] Equation (59) hints that the canonical momentum $\vec{p} = -i\hbar\nabla$ must be promoted to a new momentum[33]: $-\mathrm{i}\hbar\nabla + e\vec{A} + k_{\mathrm{SO}}\hbar(\hat{z}\times\vec{\sigma})$.

$$\nabla \to \boldsymbol{D} = \nabla + \mathrm{i}\frac{e}{\hbar}\vec{A} + \mathrm{i}k_{\mathrm{SO}}(\hat{z}\times\vec{\sigma}) \ , \tag{60}$$

where, $\boldsymbol{D}$ denotes the covariant derivative.

6.6 An additional contribution to the probability current

It should be noted that in the step from Eq. (58) to (59), an additional term with vanishing divergence could be added to the probability current, such as the curl of a vector field. The electromagnetic theory hints that the spin could induce an additional term to the probability current. A magnetized sample produces a magnetic field.[32] The volumetric electric current density of a magnetized sample is

$$\vec{\jmath}_e = \nabla \times \vec{M} \ , \tag{61}$$

where $\vec{M}$ is the magnetization. The density of the magnetic moment of the electron is proportional to the spin:

$$\vec{M} = -\mu_B \Psi^\dagger \vec{\sigma} \Psi \ , \tag{62}$$

where μ_B is the Bohr magneton. Applying (61) to (62), and dividing by the electron's charge to obtain the probability current, one obtains that

$$\vec{\jmath} = \frac{\hbar}{2m}\nabla \times (\Psi^\dagger \vec{\sigma}\Psi) \ . \tag{63}$$

The steps followed in this subsection until now do not constitute a rigorous proof, but they hint the existence of an additional term to the density current. In order to derive the value of the term induced by the magnetic moment, the classical Hamiltonian of a particle in the presence of a magnetic vector potential must be studied:

$$H_{\mathrm{cl}}(\vec{r},\vec{p},\vec{A}) = \frac{1}{2m}(\vec{p}-q\vec{A})^2 + V(\vec{r}) \; . \tag{64}$$

A small change in the vector potential induces a small change in the Hamiltonian, [34]

$$\delta H_{\mathrm{cl}} = \frac{-q}{m}(\vec{p}-q\vec{A})\cdot\delta\vec{A} = -q\dot{\vec{r}}\cdot\delta\vec{A} = -q\int d^3r'\vec{\jmath}(\vec{r}')\cdot\delta\vec{A}(\vec{r}') \; . \tag{65}$$

The classical Hamiltonian can be identified with the mean value of the quantum Hamiltonian, [35]

$$H_{\mathrm{cl}} = \int d^3r'\Psi^\dagger H_{\mathrm{qu}}\Psi \; . \tag{66}$$

Applying (66),

$$\delta H_{\mathrm{cl}} = \int d^3r' \left[\frac{-\mathrm{i}e\hbar}{2m}(\Psi^\dagger\nabla\Psi - \nabla\Psi^\dagger\Psi) + \frac{e^2}{m}\vec{A}\Psi^\dagger\Psi + \frac{\hbar k_{\mathrm{SO}}e}{m}\Psi^\dagger(\hat{z}\times\vec{\sigma})\Psi + \mu_B\nabla\times(\Psi^\dagger\vec{\sigma}\Psi)\right]\cdot\delta\vec{A} \; . \tag{67}$$

Comparing (65) to (67), the real expression for the probability current is obtained:

$$\vec{\jmath} = \frac{-\mathrm{i}\hbar}{2m}[\Psi^\dagger\nabla\Psi - \nabla\Psi^\dagger\Psi + 2\mathrm{i}\frac{e}{\hbar}\vec{A}\Psi^\dagger\Psi + 2\mathrm{i}k_{\mathrm{SO}}\Psi^\dagger(\hat{z}\times\vec{\sigma})\Psi + \mathrm{i}\nabla\times(\Psi^\dagger\vec{\sigma}\Psi)] \; . \tag{68}$$

The last term in Eq. (68) is not present in (59). However, since it is the curl of a vector, both expressions fulfill the continuity equation. The covariant derivative used should be then be

$$\nabla \to \boldsymbol{D} = \nabla + \mathrm{i}\frac{e}{\hbar}\vec{A} + \mathrm{i}k_{\mathrm{SO}}(\hat{z}\times\vec{\sigma}) + \mathrm{i}\nabla\times\vec{\sigma} \; . \tag{69}$$

6.7 Imposing boundary conditions

Kirchhoff boundary conditions must be applied to obtain the wavefunction of the system. The two requirements are the continuity of the wavefunction and no net flux at the vertices, since the probability density is constant for any eigenstate.

The continuity of the probability current at a vertex α which is not connected to the input or output lead is satisfied by the equivalent expressions

$$\sum_{\langle\alpha,\beta\rangle}\hat{\gamma}_{\alpha\beta}\cdot\boldsymbol{D}\boldsymbol{\Psi}_{\alpha\beta}\Big|_{r=0} = \boldsymbol{0} \; , \tag{70a}$$

$$\sum_{\langle\alpha,\beta\rangle}\left(\frac{\partial}{\partial r} + \mathrm{i}\frac{e}{\hbar}\vec{A}\cdot\hat{\gamma}_{\alpha\beta} + \mathrm{i}k_{\mathrm{SO}}(\hat{\gamma}_{\alpha\beta}\times\hat{z})\cdot\vec{\sigma}\right)\boldsymbol{\Psi}_{\alpha\beta}\Big|_{r=0} = \boldsymbol{0} \; . \tag{70b}$$

The sum $\sum_{\langle\alpha,\beta\rangle}$ runs over all the vertices β which are connected to α. Note that for the last term in 69, $\hat{\gamma}_{\alpha\beta}\cdot(\nabla\times\vec{\sigma})$ vanishes for a wire, so either of the two expressions for the covariant derivative (60) or (69) can be used.

If the vertices of the polygon are labeled clockwise, starting from 0 at the vertex connected to the input lead, the equations that describe the continuity of the probability current for the input and output vertices are

$$\sum_{\langle 0,\beta\rangle}\left(\frac{\partial}{\partial r}+\mathrm{i}\frac{e}{\hbar}\vec{A}\cdot\hat{\gamma}_{0,\beta}+\mathrm{i}k_{\mathrm{SO}}(\hat{\gamma}_{0,\beta}\times\hat{z})\cdot\vec{\sigma}\right)\boldsymbol{\Psi}_{0,\beta}\Big|_{r=0}-\frac{\partial\boldsymbol{\Psi}_{\mathrm{in}}}{\partial r}\Big|_{r=0}=\mathbf{0} \tag{71}$$

$$\sum_{\langle N/2,\beta\rangle}\left(\frac{\partial}{\partial r}+\mathrm{i}\frac{e}{\hbar}\vec{A}\cdot\hat{\gamma}_{N/2,\beta}+\mathrm{i}k_{\mathrm{SO}}(\hat{\gamma}_{N/2,\beta}\times\hat{z})\cdot\vec{\sigma}\right)\boldsymbol{\Psi}_{N/2,\beta}\Big|_{r=0}+\frac{\partial\boldsymbol{\Psi}_{\mathrm{out}}}{\partial r}\Big|_{r=0}=\mathbf{0} \tag{72}$$

respectively. The input/output leads are not subject to SO coupling, and the magnetic vector potential is perpendicular to the leads, so the ordinary derivative must be used. Equations (70-72) can be rewritten as [36]

$$\boldsymbol{M}_{\alpha\alpha}\boldsymbol{\Psi}_{\alpha}+\sum_{\langle\alpha,\beta\rangle}\boldsymbol{M}_{\alpha\beta}\boldsymbol{\Psi}_{\beta}=0\,, \tag{73}$$

$$\boldsymbol{M}_{0,0}\boldsymbol{\Psi}_{0}+\sum_{\langle 0,\beta\rangle}\boldsymbol{M}_{0,\beta}\boldsymbol{\Psi}_{\beta}=-\mathrm{i}(\boldsymbol{\chi}_{\sigma}-\sum_{\sigma'}r_{\sigma'\sigma}\boldsymbol{\chi}_{\sigma'})\,, \tag{74}$$

$$\boldsymbol{M}_{N/2,N/2}\boldsymbol{\Psi}_{N/2}+\sum_{\langle N/2,\beta\rangle}\boldsymbol{M}_{N/2,\beta}\boldsymbol{\Psi}_{\beta}=\mathrm{i}\sum_{\sigma'}t_{\sigma'\sigma}\boldsymbol{\chi}_{\sigma'}\,, \tag{75}$$

where

$$\boldsymbol{M}_{\alpha\alpha}=\sum_{\langle\alpha,\beta\rangle}\cot(kl)\,, \tag{76}$$

$$\boldsymbol{M}_{\alpha\beta}=-\frac{\mathrm{e}^{\mathrm{i}f(l)}\mathrm{e}^{\mathrm{i}(\hat{\gamma}_{\alpha\beta}\times\hat{z})\cdot\vec{\sigma}k_{\mathrm{SO}}l}}{\sin(kl)}\,. \tag{77}$$

In addition, the wave function must be continuous at the endpoints of the input and output leads:

$$\boldsymbol{\chi}_{\sigma}+\sum_{\sigma'}r_{\sigma'\sigma}\boldsymbol{\chi}_{\sigma'}=\boldsymbol{\Psi}_{0}\,, \tag{78}$$

$$\sum_{\sigma'}t_{\sigma'\sigma}\boldsymbol{\chi}_{\sigma'}=\boldsymbol{\Psi}_{N/2}\,. \tag{79}$$

Replacing $r_{\sigma'\sigma}$ and $t_{\sigma'\sigma}$ from (78-79) into (73-75) we obtain a linear nonhomogeneous equation system with 2N variables, two per each vertex. The equation system can be expressed matricially as[2]

$$\begin{bmatrix}\boldsymbol{M}_{0,0}-\mathrm{i} & \boldsymbol{M}_{0,1} & \mathbf{0} & \cdots & \mathbf{0} & \cdots & \boldsymbol{M}_{0,N-1}\\ \boldsymbol{M}_{1,0} & \boldsymbol{M}_{1,1} & \boldsymbol{M}_{1,2} & \cdots & \mathbf{0} & \cdots & \mathbf{0}\\ \mathbf{0} & \boldsymbol{M}_{2,1} & \boldsymbol{M}_{2,2} & \cdots & \mathbf{0} & \cdots & \mathbf{0}\\ \vdots & \vdots & \vdots & \ddots & \vdots & \ddots & \vdots\\ \mathbf{0} & \mathbf{0} & \mathbf{0} & \cdots & \boldsymbol{M}_{N/2,N/2}-\mathrm{i} & \cdots & \mathbf{0}\\ \vdots & \vdots & \vdots & \ddots & \vdots & \ddots & \vdots\\ \boldsymbol{M}_{N-1,0} & \mathbf{0} & \mathbf{0} & \cdots & \mathbf{0} & \cdots & \boldsymbol{M}_{N-1,N-1}\end{bmatrix}\begin{bmatrix}\boldsymbol{\Psi}_{0}\\ \boldsymbol{\Psi}_{1}\\ \boldsymbol{\Psi}_{2}\\ \vdots\\ \boldsymbol{\Psi}_{N/2}\\ \vdots\\ \boldsymbol{\Psi}_{N-1}\end{bmatrix}=\begin{bmatrix}-2\mathrm{i}\boldsymbol{\chi}_{\sigma}\\ \mathbf{0}\\ \mathbf{0}\\ \vdots\\ \mathbf{0}\\ \vdots\\ \mathbf{0}\end{bmatrix} \tag{80}$$

[2]Note that $\boldsymbol{M}_{j,k}$ is a 2×2 tensor and $\boldsymbol{\Psi}_{j}$ is a spinor

At this point computational methods could be used to solve equation system (80) and obtain the value of the spinor at the vertices $\mathbf{\Psi}_\alpha$. Equations (50,52-53) provide the value of the wave function at any given point. In addition, the reflection and transmission coefficients $r_{\sigma'\sigma}$ and $t_{\sigma'\sigma}$ can be obtained through (78-79). The conductance is given by Landauer formula:

$$G = \frac{G_0}{2} \operatorname{Tr} TT^\dagger \tag{81}$$

where T is the transmission matrix and $G_0 = 2e^2/\hbar$ is the conductance quantum. [37]

7 Simulation of a 1D ring

A 1D ring is a ring where electrons can be described with a single coordinate: the azimuth angle. The electrons are therefore constrained to a constant radius. Using the method developed in Sec. 6, the conductance of the ring can be calculated for different values of k_{SO}.

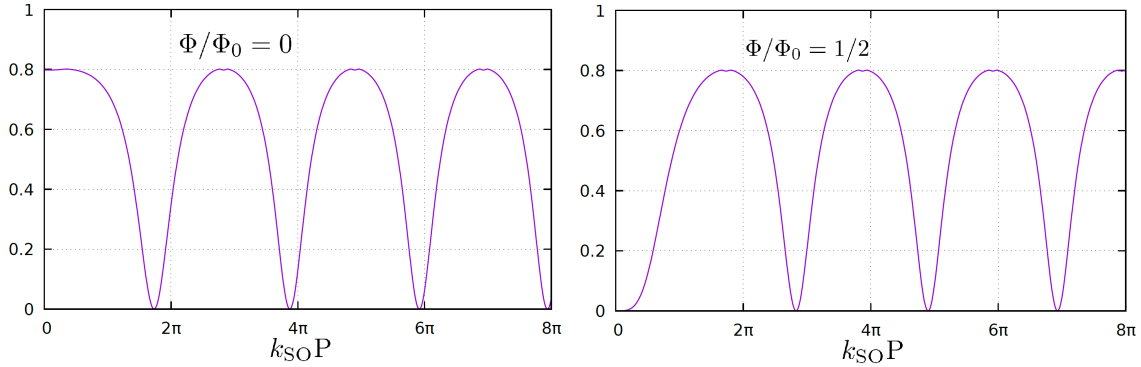

Figure 11: Conductance of a quantum ring averaged over values of the momentum $k \in [0, \pi/\mathrm{P}]$ and input channel, as a function of the SO coupling strength multiplied by the perimeter. The conductance is given in units of $2e^2/h$. The left image corresponds to a flux free case, while the right image corresponds to the half a flux quantum.

Figure 11 plots the value of the averaged value of the conductance as a function of the SO coupling strength. The conductance has been averaged for values of the momentum $k \in [0, \pi/\mathrm{P}]$, since the conductance is periodic in k with period $\mathrm{T}_k = 2\pi/\mathrm{P}$. The conductance displays quasiperiodic oscillations for $k_{\mathrm{SO}}\mathrm{P}$ of period approaching 2π as $k_{\mathrm{SO}}\mathrm{P}$ tends to infinity. When the dimensionless SO coupling strength tends to infinity, we obtain the adiabatic limit in which the spin is aligned with the effective magnetic field during transport and Berry phases arise. [26]

At half a quantum flux, the oscillation of the conductance is inversed, so that there is a destructive interference for $k_{\mathrm{SO}} = 0$. The position of the maxima and minima are interchanged.

7.1 Comparison of different polygons

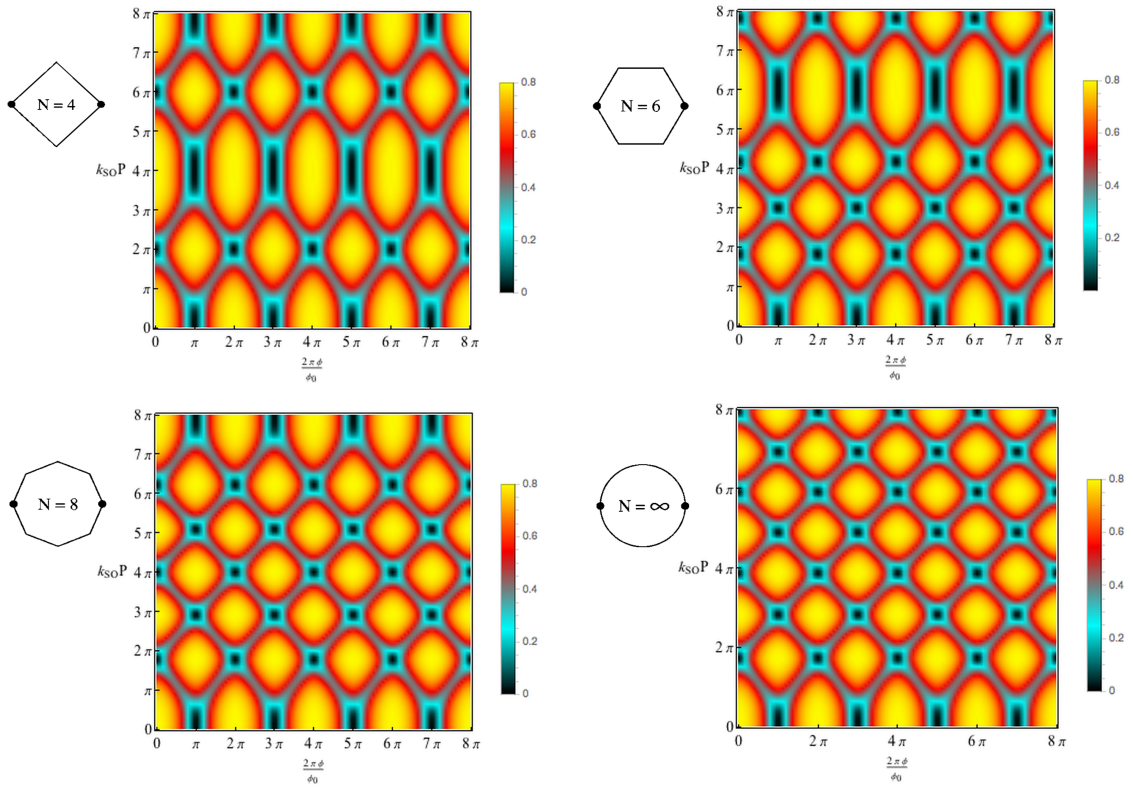

Figure 12: Conductance of different polygons averaged over values of the momentum $k \in [0, \pi/\mathrm{P}]$ and input channel, as a function of the SO coupling strength multiplied by the perimeter and the dimensionless flux.

Figure 12 plots the conductance of different polygons in units of $2e^2/h$. It should be noted that for all systems the conductance is periodic for the magnetic flux, where the period is the flux quantum. The results of Fig. 11 are recovered from Fig. 12 cutting the graph at zero and half a flux quantum.

It can be noted that there are broader and narrower maxima for different values of $k_{\mathrm{SO}}\mathrm{P}$. The periodicity of the broader maxima is related to the length of the sides of the polygon, where the period is $\pi/l = n\pi/\mathrm{P}$. This period tends to infinity as the number of sides tends to infinity, so there are no broad maxima for the ring, apart from the one located at the origin.

The periodicity of the narrow maxima is related to the length of the perimeter, therefore, it is similar for all polygons. The quasiperiod ranges from 4π for the case of the square to 2π as the number of sides increases.

8 Inplane magnetic field

8.1 RSOI and Zeeman field in a wire

Let a quantum wire be subject to Rashba SO coupling and a constant Zeeman field $\vec{B}$.

$$\hat{H} = \frac{1}{2m}\vec{p}^{\,2} + \frac{\hbar k_{\mathrm{SO}}}{m}(\vec{p}\times\hat{z})\cdot\vec{\sigma} + \mu\vec{B}\cdot\vec{\sigma}\,, \tag{82}$$

where μ is the magnetic moment of the particle. For electrons, the magnetic moment is the Bohr magneton $\mu_B = \frac{e\hbar}{2m}$. The interaction of the Zeeman field with the spin of the electron is described by the last term in Eq. (82). Both the Rashba and the Zeeman term are expressed in terms of the Pauli matrices, thus, they are SU(2) terms. Unlike the Rashba term, the Zeeman term does not contain the momentum, so it can not be gauged out from the equation.

Let the wire and the direction of the Zeeman field lie in the xy-plane, where the wire forms and angle γ with the x axis, $\hat{\gamma} = (\cos\gamma, \sin\gamma, 0)$ and the field is given by $\vec{B} = B(\cos\alpha, \sin\alpha, 0)$. Then, the Hamiltonian of the system reads

$$\begin{aligned}\hat{H} =& \frac{p_\gamma^2}{2m} + \frac{\hbar k_{\mathrm{SO}}}{m}p_\gamma(\hat{\gamma}\times\hat{z})\cdot\vec{\sigma} + \mu B(\vec{\alpha}\cdot\vec{\sigma}) \\ =& -\frac{\hbar^2}{2m}\frac{\partial^2}{\partial r^2} + \frac{\hbar^2 k_{\mathrm{SO}}}{m}\begin{pmatrix}0 & \mathrm{e}^{-\mathrm{i}\gamma}\\ -\mathrm{e}^{\mathrm{i}\gamma} & 0\end{pmatrix}\frac{\partial}{\partial r} + \mu B\begin{pmatrix}0 & \mathrm{e}^{-\mathrm{i}\alpha}\\ \mathrm{e}^{\mathrm{i}\alpha} & 0\end{pmatrix}\,.\end{aligned} \tag{83}$$

We can solve the Fourier transform of the Schrödinger equation. Using a spinorial wave function with a plane wave factor,

$$\boldsymbol{\Psi} = \boldsymbol{\chi}\mathrm{e}^{\mathrm{i}kr}\,, \tag{84}$$

where $\boldsymbol{\chi}$ is a two component spinor and k is the momentum, the Hamiltonian can be reduced to the following matrix:

$$\hat{H} = \begin{pmatrix}\frac{\hbar^2k^2}{2m} & \mathcal{M}\\ \mathcal{M}^* & \frac{\hbar^2k^2}{2m}\end{pmatrix}\,, \tag{85}$$

where $\mathcal{M} = (\mu B\cos\alpha + \frac{\hbar^2 k_{\mathrm{SO}}k}{m}\sin\gamma) + \mathrm{i}(-\mu B\sin\alpha + \frac{\hbar^2 k_{\mathrm{SO}}k}{m}\cos\gamma)$. The modulus and angle of $\mathcal{M} = |\mathcal{M}|\mathrm{e}^{-\mathrm{i}\theta}$ can be written as

$$|\mathcal{M}| = \sqrt{\mu^2B^2 + \frac{\hbar^4k_{\mathrm{SO}}^2k^2}{m^2} + 2\frac{\hbar^2k_{\mathrm{SO}}k}{m}\mu B\sin(\gamma-\alpha)} \tag{86a}$$

$$\theta = \arctan\frac{\mu B\sin\alpha - \frac{\hbar^2k_{\mathrm{SO}}k}{m}\cos\gamma}{\mu B\cos\alpha + \frac{\hbar^2k_{\mathrm{SO}}k}{m}\sin\gamma}\,. \tag{86b}$$

The eigenvalues and eigenfunctions of the Hamiltonian are

$$\varepsilon_\pm = \frac{\hbar^2k^2}{2m} \pm |\mathcal{M}|\,, \tag{87}$$

$$\boldsymbol{\Psi} = \frac{1}{\sqrt{2}}\begin{pmatrix}\mathrm{e}^{-\mathrm{i}\theta/2}\\ \pm\mathrm{e}^{\mathrm{i}\theta/2}\end{pmatrix}\mathrm{e}^{\mathrm{i}kr}\,. \tag{88}$$

For a high enough value of the energy, the system will have four available propagating states, where two states propagate forward and two backward. The momenta corresponding to such states are labeled as k_+^{F}, k_-^{F}, k_+^{B} and k_-^{B}, with respective angles θ_+^{F}, θ_-^{F}, θ_+^{B} and θ_-^{B}. Here, the subscript $\pm$ indicates the energy band in which the state is located at, while the superscript indicates the propagation direction.

The system has two energy bands. The spin direction of each band is given by the spinor in (88). The spin direction lies in the xy plane, and it remains constant along the wire. The azimuth angle for the upper band, ε_+, is equal to θ_+. However, for the lower band, the azimuth angle is equal to $\theta_- + \pi$.

8.2 The spin dynamics

As we have seen in Sec. 8.1, at high energies there are four available states. It is useful to expand the eigenvectors $|s\rangle$ of spin operator $\hat{S}_z$ into the bases formed by the available states $\{|\boldsymbol{v}_\pm^{\mathrm{F}}\rangle\}$ and $\{|\boldsymbol{v}_\pm^{\mathrm{B}}\rangle\}$:

$$|\boldsymbol{v}_\alpha^\gamma\rangle = \frac{1}{\sqrt{2}} \begin{pmatrix} \mathrm{e}^{-\mathrm{i}\theta_\alpha^\gamma/2} \\ \alpha \mathrm{e}^{\mathrm{i}\theta_\alpha^\gamma/2} \end{pmatrix} \tag{89}$$

that are not orthogonal, but fulfill the relation

$$\langle \boldsymbol{v}_\alpha^\gamma | \boldsymbol{v}_\beta^\delta \rangle = \frac{1}{2} \left(\mathrm{e}^{\mathrm{i}(\theta_\alpha^\gamma - \theta_\beta^\delta)/2} + \alpha\beta \mathrm{e}^{-\mathrm{i}(\theta_\alpha^\gamma - \theta_\beta^\delta)/2} \right) = \begin{cases} \cos \frac{\theta_\alpha^\gamma - \theta_\beta^\delta}{2} & \text{if } \alpha = \beta \\ \mathrm{i} \sin \frac{\theta_\alpha^\gamma - \theta_\beta^\delta}{2} & \text{otherwise} \end{cases} . \tag{90}$$

In order to expand a generic vector into a non orthogonal basis $|\boldsymbol{u}\rangle = c_1|\boldsymbol{v}_1\rangle + c_2|\boldsymbol{v}_2\rangle$, we can make use of the Gram matrix:

$$\boldsymbol{M} = \begin{pmatrix} \langle \boldsymbol{v}_1 | \boldsymbol{v}_1 \rangle & \langle \boldsymbol{v}_1 | \boldsymbol{v}_2 \rangle \\ \langle \boldsymbol{v}_2 | \boldsymbol{v}_1 \rangle & \langle \boldsymbol{v}_2 | \boldsymbol{v}_2 \rangle \end{pmatrix} . \tag{91}$$

Taking inner products of $\langle \boldsymbol{v}_i|$ with $|\boldsymbol{u}\rangle$

$$\boldsymbol{u} = \boldsymbol{M}\boldsymbol{c} \,, \tag{92}$$

where

$$\boldsymbol{u} = \begin{pmatrix} \langle \boldsymbol{v}_1 | \boldsymbol{u} \rangle \\ \langle \boldsymbol{v}_2 | \boldsymbol{u} \rangle \end{pmatrix}, \quad \boldsymbol{c} = \begin{pmatrix} c_1 \\ c_2 \end{pmatrix} . \tag{93}$$

Taking the inverse of the Gram matrix, we obtain the coefficients c_1 and c_2. The two spin eigenstates $|s\rangle$ can therefore be written as

$$|\uparrow\rangle = \begin{pmatrix} 1 \\ 0 \end{pmatrix} = \frac{1}{\sqrt{2}\cos\frac{\theta_+ - \theta_-}{2}} \left(\mathrm{e}^{\mathrm{i}\theta_-/2} |\boldsymbol{v}_+\rangle + \mathrm{e}^{\mathrm{i}\theta_+/2} |\boldsymbol{v}_-\rangle \right) , \tag{94a}$$

$$|\downarrow\rangle = \begin{pmatrix} 0 \\ 1 \end{pmatrix} = \frac{1}{\sqrt{2}\cos\frac{\theta_+ - \theta_-}{2}} \left(\mathrm{e}^{-\mathrm{i}\theta_-/2} |\boldsymbol{v}_+\rangle - \mathrm{e}^{-\mathrm{i}\theta_+/2} |\boldsymbol{v}_-\rangle \right) . \tag{94b}$$

For the sake of simplicity, the superscripts F/B have been omitted in (94). Knowing that states (89) acquire a dynamical phase when travelling a distance r, given by (88), we can write the spatial evolution of the states $|s\rangle$ as

$$|f\rangle_\uparrow = \frac{1}{\sqrt{2}\cos\frac{\theta_+-\theta_-}{2}}\left(\mathrm{e}^{\mathrm{i}\theta_-/2}\mathrm{e}^{\mathrm{i}k_+r}|\boldsymbol{v}_+\rangle + \mathrm{e}^{\mathrm{i}\theta_+/2}\mathrm{e}^{\mathrm{i}k_-r}|\boldsymbol{v}_-\rangle\right) , \tag{95a}$$

$$|f\rangle_\downarrow = \frac{1}{\sqrt{2}\cos\frac{\theta_+-\theta_-}{2}}\left(\mathrm{e}^{-\mathrm{i}\theta_-/2}\mathrm{e}^{\mathrm{i}k_+r}|\boldsymbol{v}_+\rangle - \mathrm{e}^{-\mathrm{i}\theta_+/2}\mathrm{e}^{\mathrm{i}k_-r}|\boldsymbol{v}_-\rangle\right) . \tag{95b}$$

The states $|f\rangle_{\uparrow/\downarrow}$ can be expanded into their up and down components through the transfer matrix

$$\hat{\boldsymbol{\mathcal{T}}} = \begin{pmatrix} \langle\uparrow|f\rangle_\uparrow & \langle\downarrow|f\rangle_\uparrow \\ \langle\uparrow|f\rangle_\downarrow & \langle\downarrow|f\rangle_\downarrow \end{pmatrix} . \tag{96}$$

Finally, the states are given by

$$\begin{pmatrix} |f\rangle_\uparrow \\ |f\rangle_\downarrow \end{pmatrix} = \hat{\boldsymbol{\mathcal{T}}}\begin{pmatrix} |\uparrow\rangle \\ |\downarrow\rangle \end{pmatrix} = \frac{1}{\cos\frac{\Delta\theta}{2}}\begin{pmatrix} \cos\frac{\Delta k r-\Delta\theta}{2} & \mathrm{i}\mathrm{e}^{\mathrm{i}\theta}\sin\frac{\Delta k r}{2} \\ \mathrm{i}\mathrm{e}^{-\mathrm{i}\theta}\sin\frac{\Delta k r}{2} & \cos\frac{\Delta k r+\Delta\theta}{2} \end{pmatrix}\begin{pmatrix} |\uparrow\rangle \\ |\downarrow\rangle \end{pmatrix}\mathrm{e}^{\mathrm{i}kr} . \tag{97}$$

Here we have introduced the parameters $k = \frac{k_++k_-}{2}$, $\Delta k = k_+-k_-$, $\theta = \frac{\theta_++\theta_-}{2}$ and $\Delta\theta = \theta_+-\theta_-$. Note that these four parameters will depend on the basis used $\{|\boldsymbol{v}^{\mathrm{F}}_\pm\rangle\}$ or $\{|\boldsymbol{v}^{\mathrm{B}}_\pm\rangle\}$.

Let us assume that we are given the value of a state at $r = 0$, and we know which are the forward and backward components of the state

$$\begin{aligned} \boldsymbol{\Psi}(0) =& \boldsymbol{\Psi}^{\mathrm{F}}(0) + \boldsymbol{\Psi}^{\mathrm{B}}(0) \\ =& \sum_{\gamma\in\{\mathrm{F},\mathrm{B}\}} \chi^\gamma_\uparrow|\uparrow\rangle + \chi^\gamma_\downarrow|\downarrow\rangle . \end{aligned} \tag{98}$$

The spatial evolution of the state can be written as

$$\begin{aligned} \boldsymbol{\Psi}(r) =& \boldsymbol{\Psi}^{\mathrm{F}}(r) + \boldsymbol{\Psi}^{\mathrm{B}}(r) \\ =& \sum_{\gamma\in\{\mathrm{F},\mathrm{B}\}} \chi^\gamma_\uparrow|f\rangle^\gamma_\uparrow + \chi^\gamma_\downarrow|f\rangle^\gamma_\downarrow \end{aligned} \tag{99}$$

Applying (97) to (99), we obtain that

$$\begin{aligned} \boldsymbol{\Psi}^\gamma(r) =& \hat{\boldsymbol{\mathcal{R}}}^\gamma\mathrm{e}^{\mathrm{i}k^\gamma r}\boldsymbol{\Psi}^\gamma(0) \\ =& \frac{1}{\cos\frac{\Delta\theta^\gamma}{2}}\begin{pmatrix} \cos\frac{\Delta k^\gamma r-\Delta\theta^\gamma}{2} & \mathrm{i}\mathrm{e}^{-\mathrm{i}\theta^\gamma}\sin\frac{\Delta k^\gamma r}{2} \\ \mathrm{i}\mathrm{e}^{\mathrm{i}\theta^\gamma}\sin\frac{\Delta k^\gamma r}{2} & \cos\frac{\Delta k^\gamma r+\Delta\theta^\gamma}{2} \end{pmatrix}\mathrm{e}^{\mathrm{i}k^\gamma r}\boldsymbol{\Psi}^\gamma(0) \\ =& \left[\mathrm{e}^{\mathrm{i}\hat{\theta}^\gamma\cdot\vec{\sigma}\frac{\Delta k^\gamma r}{2}} + \sin\frac{\Delta k^\gamma r}{2}\tan\frac{\Delta\theta^\gamma}{2}\sigma_z\right]\mathrm{e}^{\mathrm{i}k^\gamma r}\boldsymbol{\Psi}^\gamma(0) , \end{aligned} \tag{100}$$

where $\hat{\boldsymbol{\mathcal{R}}} = \hat{\boldsymbol{\mathcal{T}}}^\top$ is the transpose of the transfer matrix, excluding the $\mathrm{e}^{\mathrm{i}k^\gamma r}$ factor.

8.3 $k_{\mathrm{SO}} \neq 0$ and $B = 0$ case

In the limit of zero Zeeman field, $|\mathcal{M}| = \frac{\hbar^2 k_{\mathrm{SO}}|k|}{m}$ and $\theta = \arctan \frac{-k\cos\gamma}{k\sin\gamma}$. The energy in Eq. (87) then reduces to

$$\varepsilon_{\pm} = \frac{\hbar^2 k^2}{2m} \pm \frac{\hbar^2 k_{\mathrm{SO}}|k|}{m} \,. \tag{101}$$

The momenta for a fixed Fermi energy $\varepsilon_{\mathrm{F}} = \frac{\hbar^2 k_{\mathrm{F}}^2}{2m}$ are $|k_{\pm}| = \sqrt{k_{\mathrm{F}}^2 + k_{\mathrm{SO}}^2} \mp k_{\mathrm{SO}}$, where the forward (backward) momenta are positive (negative).

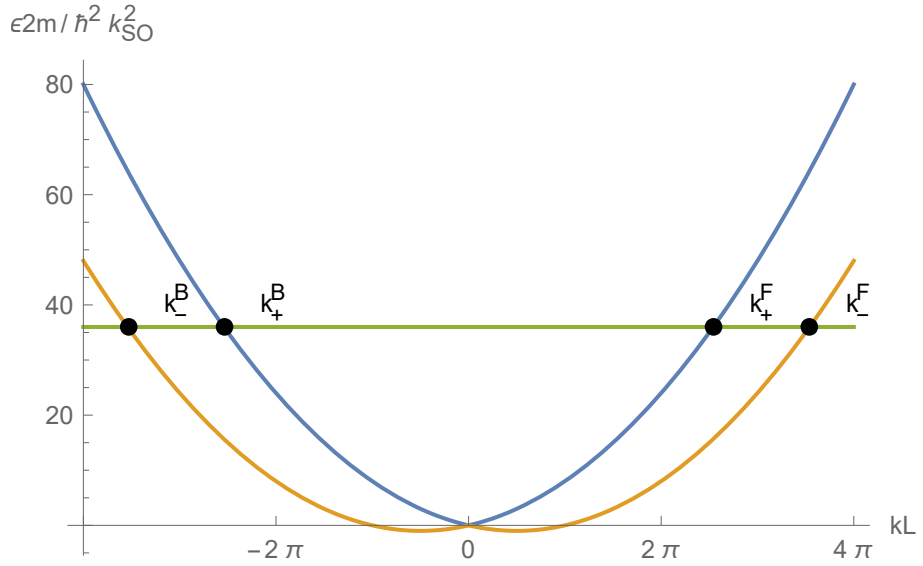

Figure 13: Upper (blue) an lower (orange) bands of the Zeeman field free system as a function of the momentum. The momenta for a certain Fermi energy are k_+^{F}, k_-^{F}, k_+^{B} and k_-^{B}.

The energy as a function of the momentum is plotted in Fig. 13. The energy bands are symmetric with respect to $k = 0$, where the upper and lower band intersect. The difference between the momenta of each band is equal to $2k_{\mathrm{SO}}$ for any value of the energy. Equation (101) tells us that the energy diagram is independent of γ.

In order to calculate the angles, we must take into account the sign of their respective momenta. The angles are

$$\theta_{\pm}^{\mathrm{F}} = \arctan \frac{-\cos\gamma}{\sin\gamma} = \gamma - \frac{\pi}{2} \,, \tag{102a}$$

$$\theta_{\pm}^{\mathrm{B}} = \arctan \frac{\cos\gamma}{-\sin\gamma} = \gamma + \frac{\pi}{2} \,. \tag{102b}$$

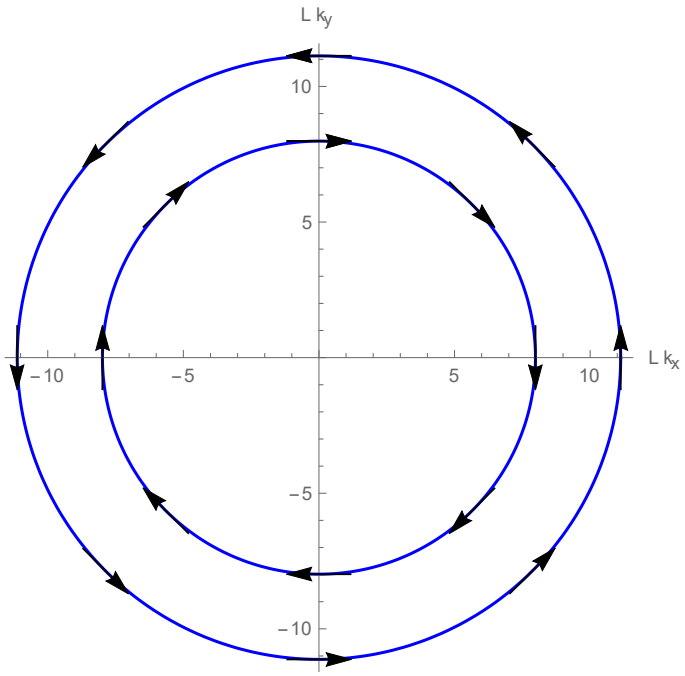

Figure 14: Spin direction at the Fermi contour as a function of the wire's direction, which is given by k_x and k_y.

The spin orientation for each state as a function of the wire's direction γ is presented in Fig. 14. Since the modulus of the momentum does not depend on the direction of the wire, the energy bands form two circles in the momentum space. The spin states of the upper and lower bands for a given direction have opposite direction. The spin is always perpendicular to the travel direction, so that it is aligned to the effective magnetic field arising from the SO coupling. Applying this result to a 1D ring, we can conclude that the spin would have a radial direction, that is to say, it would align with the effective magnetic field.

The average and difference parameters defined in Sec. 8.2 are $k^{\mathrm{F}} = -k^{\mathrm{B}} = \sqrt{k_{\mathrm{F}}^2 + k_{\mathrm{SO}}^2}$, $\Delta k^{\mathrm{F}} = -\Delta k^{\mathrm{B}} = -2k_{\mathrm{SO}}$, $\theta^{\mathrm{F}} = \gamma - \frac{\pi}{2}$, $\theta^{\mathrm{B}} = \gamma + \frac{\pi}{2}$ and $\Delta\theta^{\mathrm{F}} = \Delta\theta^{\mathrm{B}} = 0$.

The matrix $\hat{\boldsymbol{\mathcal{R}}}$ takes the simple form

$$\hat{\boldsymbol{\mathcal{R}}} = \begin{pmatrix} \cos k_{\mathrm{SO}} r & \mathrm{e}^{-\mathrm{i}\gamma} \sin k_{\mathrm{SO}} r \\ -\mathrm{e}^{\mathrm{i}\gamma} \sin k_{\mathrm{SO}} r & \cos k_{\mathrm{SO}} r \end{pmatrix} = \mathrm{e}^{-\mathrm{i}(\hat{\gamma}\times\hat{z})\cdot\vec{\sigma} k_{\mathrm{SO}} r} \,. \tag{103}$$

It should be noted that $\hat{\boldsymbol{\mathcal{R}}}$ has the same form for both forward and backward cases. Comparing Eq. (103) to (47), we can see that we recover the results obtained for the case where we only have Rashba SO coupling.[7;36]

8.4 $k_{\mathrm{SO}} = 0$ and $B \neq 0$ case

In the limit where there is no SO coupling, $|\mathcal{M}| = \mu B$ and $\theta = \alpha$. The kinetic and magnetic term of the Hamiltonian commute, so the energy of the system is given by

$$\varepsilon_{\pm} = \frac{\hbar^2 k^2}{2m} \pm \mu B \,. \tag{104}$$

The momenta for a fixed Fermi energy are $|k_{\pm}| = \sqrt{k_{\mathrm{F}}^2 \mp \frac{2m\mu B}{\hbar^2}}$, so $k^{\mathrm{F}} = -k^{\mathrm{B}} = \frac{1}{2}\left(\sqrt{k_{\mathrm{F}}^2 + \frac{2m\mu B}{\hbar^2}} + \sqrt{k_{\mathrm{F}}^2 - \frac{2m\mu B}{\hbar^2}}\right)$, $\Delta k^{\mathrm{F}} = -\Delta k^{\mathrm{B}} = \sqrt{k_{\mathrm{F}}^2 - \frac{2m\mu B}{\hbar^2}} - \sqrt{k_{\mathrm{F}}^2 + \frac{2m\mu B}{\hbar^2}}$, $\theta^{\mathrm{F}} = \theta^{\mathrm{B}} = \alpha$ and $\Delta\theta^{\mathrm{F}} = \Delta\theta^{\mathrm{B}} = 0$.

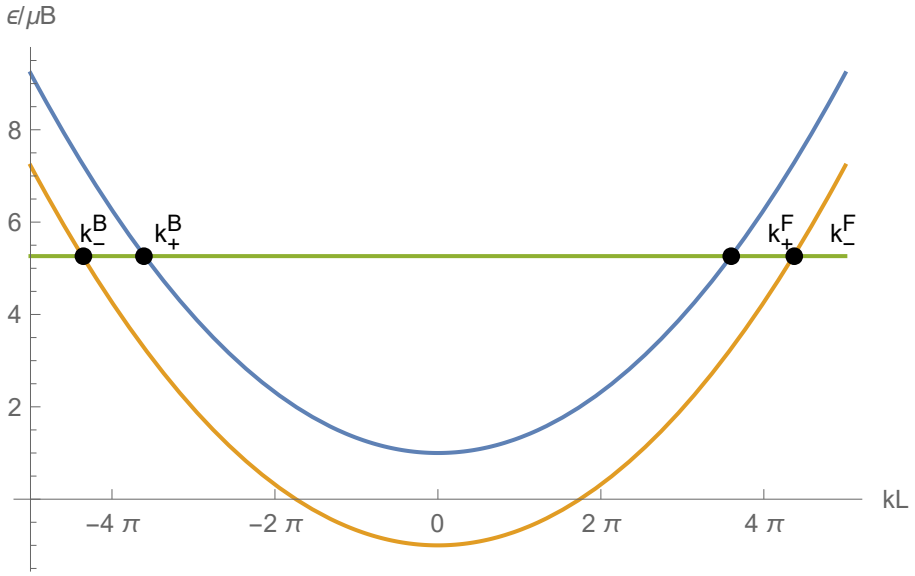

Figure 15: Upper (blue) an lower (orange) bands of the SO coupling free system as a function of the momentum.

The energy as a function of the momentum is plotted in Fig. 15. According to Eq. (104), the energy bands form two paraboloids centered at $k = 0$. This means that the momentum is independent of the wire's direction. The difference between the momenta of each band for a fixed energy decreases with k, and as ε approaches infinity the difference tends to $\Delta k = \frac{2m\mu B}{k_{\mathrm{F}}\hbar^2}$.

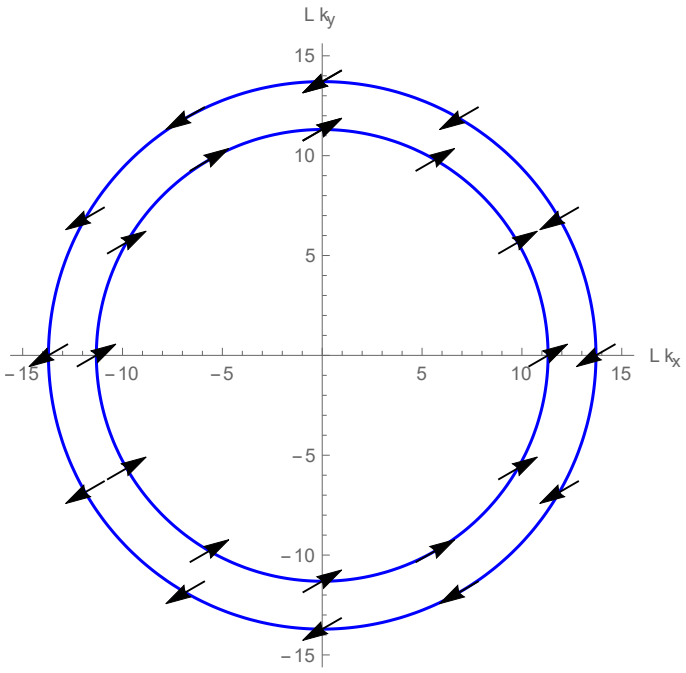

Figure 16: Spin direction as a function of the wire's direction, for each energy band. The direction of the Zeeman field is $\alpha = \frac{\pi}{6}$.

The spin direction of the states is independent of the momentum direction. In fact, the spin will always be aligned with the Zeeman field. Similar to the Zeeman field free case, the spin states of the both bands have opposite direction. The spin of the state with smaller momentum is parallel to the Zeeman field, so that the a positive magnetic energy is added to the kinetic energy. The spin of the state with higher momentum is antiparallel to the Zeeman field, so that the total energy of both states is the same.

Unlike the field free case, matrix $\hat{\boldsymbol{\mathcal{R}}}$ is different for the forward and backward components:

$$\hat{\boldsymbol{\mathcal{R}}} = \begin{pmatrix} \cos\frac{\Delta kr}{2} & \mathrm{i}e^{-\mathrm{i}\alpha}\sin\frac{\Delta kr}{2} \\ \mathrm{i}e^{\mathrm{i}\alpha}\sin\frac{\Delta kr}{2} & \cos\frac{\Delta kr}{2} \end{pmatrix} = e^{\mathrm{i}\hat{\alpha}\cdot\vec{\sigma}\frac{\Delta kr}{2}} \ . \tag{105}$$

It is worth noting that the rotation matrix is independent of the direction γ of the wire.

8.5 $k_{\mathrm{SO}} \neq 0$ and $B \neq 0$ case

For the general case, it is no longer true that the momentum is independent of the wire's direction. In addition, the states of both bands will no longer be orthogonal, but will fulfill the relation in Eq. (90).

The relation between the energy and the momentum (87) does not allow isolating the momentum. Depending on the relative strength between the SO coupling constant and the Zeeman field, the system will have a different behaviour.

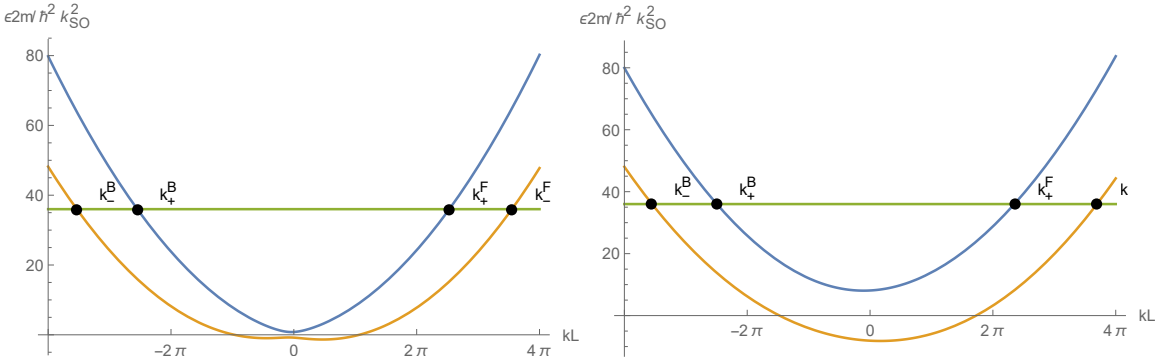

Figure 17: Energy bands for $k_{\mathrm{SO}} = \frac{\pi}{2\mathrm{L}}$, $\gamma = \pi/4$, $\alpha = \pi/6$ and Fermi momentum $k_{\mathrm{F}} = 6k_{\mathrm{SO}}$ for $\mu B = 0.81\frac{\hbar^2 k_{\mathrm{SO}}^2}{2m}$ (left) and $\mu B = 8.1\frac{\hbar^2 k_{\mathrm{SO}}^2}{2m}$ (right). Here $\mathrm{L} = 1000a_0$ is the length of the wire and a_0 the Bohr radius.

The left image in Fig. 17 corresponds to a weak Zeeman field, so it resembles the energy graph in Fig. 13. The right image corresponds to a weak SO coupling. The energy bands are no longer symmetric respect to the origin because time reversal symmetry (TRS) is broken, so the relation $k_\alpha^{\mathrm{F}} = -k_\alpha^{\mathrm{B}}$ is no longer valid.

The spin direction can be seen in Fig. 18. As the magnitude of the Zeeman field increases, the direction of the spin tends to align with the direction of the field.

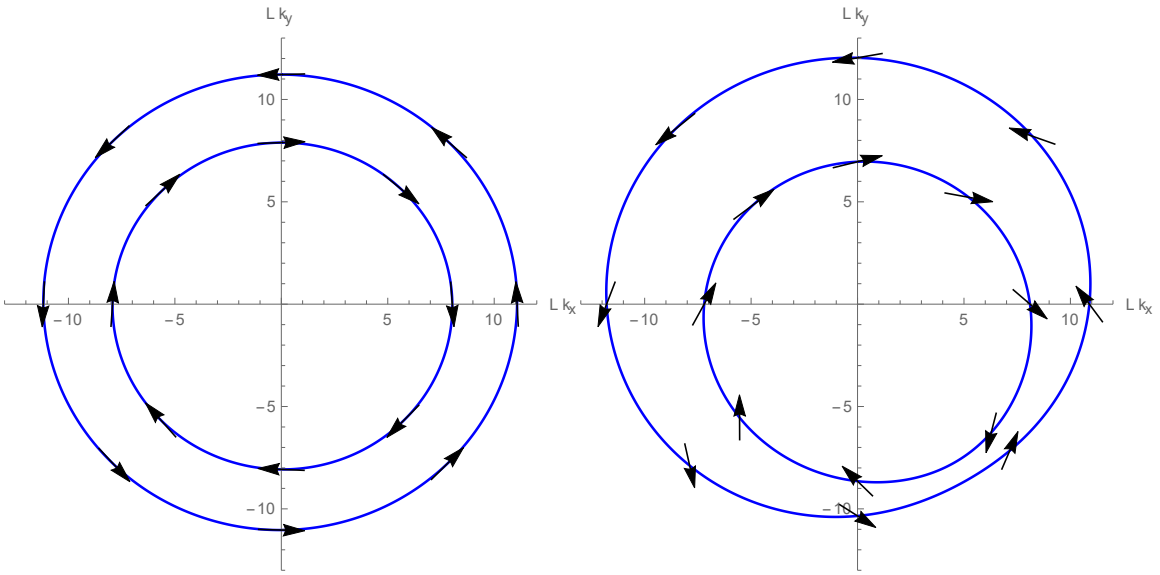

Figure 18: Spin direction as a function of the wire's direction, for each energy band. The images correspond to the parameters used in Fig. 17.

8.6 Energy band crossing

The energy band crossing between the upper and lower bands for a given k can be deduced from Eq. (87). The energy difference between both bands is given by

$$\varepsilon_+ - \varepsilon_- = 2|\mathcal{M}| \, . \tag{106}$$

It is interesting to study when the energy bands intersect. Using Eq. (86a),

$$\sqrt{\mu^2 B^2 + \frac{\hbar^4 k_{\mathrm{SO}}^2 k^2}{m^2} \mp 2\frac{\hbar^2 k_{\mathrm{SO}} k}{m}\mu B} \leq |\mathcal{M}| \leq \sqrt{\mu^2 B^2 + \frac{\hbar^4 k_{\mathrm{SO}}^2 k^2}{m^2} \pm 2\frac{\hbar^2 k_{\mathrm{SO}} k}{m}\mu B} \, , \tag{107}$$

where the upper sign corresponds to a positive momentum and the lower sign to a negative momentum. $|\mathcal{M}|$ will take all the values in the range specified by (107), depending on the angle formed by the wire and the Zeeman field. Therefore, $|\mathcal{M}|$ will only be equal to zero when $\sin(\gamma - \alpha) = \mp 1$. For this case, (86a) reduces to

$$|\mathcal{M}| = |\mu B \mp \frac{\hbar^2 k_{\mathrm{SO}} k}{m}| = 0 \tag{108}$$

When the magnitudes of the Zeeman and SO interaction are equal, and the Zeeman field is perpendicular to the wire, the energy band crossing will occur. From (87), we deduce that the band intersection will occur at $k = \pm k_{\mathrm{F}}$. Focusing on the positive momenta, k_+^{F} will be equal to k_-^{F}. As it has been argued in Sec. 8.5, Eq. (87) can not be solved analytically to obtain all the values of the momenta for the general case. However, in this case the equation simplifies to

$$\frac{\hbar^2 k_{\mathrm{F}}^2}{2m} = \frac{\hbar^2 k^2}{2m} \pm |\mu B - \frac{\hbar^2 k_{\mathrm{SO}} k}{m}| \, . \tag{109}$$

Isolating the absolute value and squaring both sides,

$$k^4 - (2k_{\mathrm{F}}^2 + 4k_{\mathrm{SO}}^2)k^2 + 8k_{\mathrm{SO}}^2 k_{\mathrm{F}} k + k_{\mathrm{F}}^4 - 4k_{\mathrm{SO}}^2 k_{\mathrm{F}}^2 = 0 \, . \tag{110}$$

We know that $k_\pm^{\mathrm{F}} = k_{\mathrm{F}}$ is a two-fold degenerate solution, so factoring the equation will give the remaining solutions $k_\pm^{\mathrm{B}} = -k_{\mathrm{F}} \pm 2k_{\mathrm{SO}}$. The angles are given by

$$\theta = \arctan \frac{(\mu B - \frac{\hbar^2 k_{\mathrm{SO}} k}{m}) \sin\alpha}{(\mu B - \frac{\hbar^2 k_{\mathrm{SO}} k}{m}) \cos\alpha} = \begin{cases} \alpha, \text{ if } \mu B > \frac{\hbar^2 k_{\mathrm{SO}} k}{m} \\ \alpha + \pi, \text{ if } \mu B < \frac{\hbar^2 k_{\mathrm{SO}} k}{m} \end{cases} \, . \tag{111}$$

The angle is not defined for $\mu B - \frac{\hbar^2 k_{\mathrm{SO}} k}{m}$, which is our case of interest. This can also be deduced from the fact that the angle is the argument of $\mathcal{M}$, which is zero when the bands intersect.

The average and momenta difference parameters are $k^{\mathrm{F}} = -k^{\mathrm{B}} = k_{\mathrm{F}}$, $\Delta k^{\mathrm{F}} = 0$ and $\Delta k^{\mathrm{B}} = 4k_{\mathrm{SO}}$. Actually, the momenta difference is maximum in one direction, while it is zero in the opposite direction. The same procedure can be followed to obtain the momenta when the degeneracy occurs for a negative momentum.

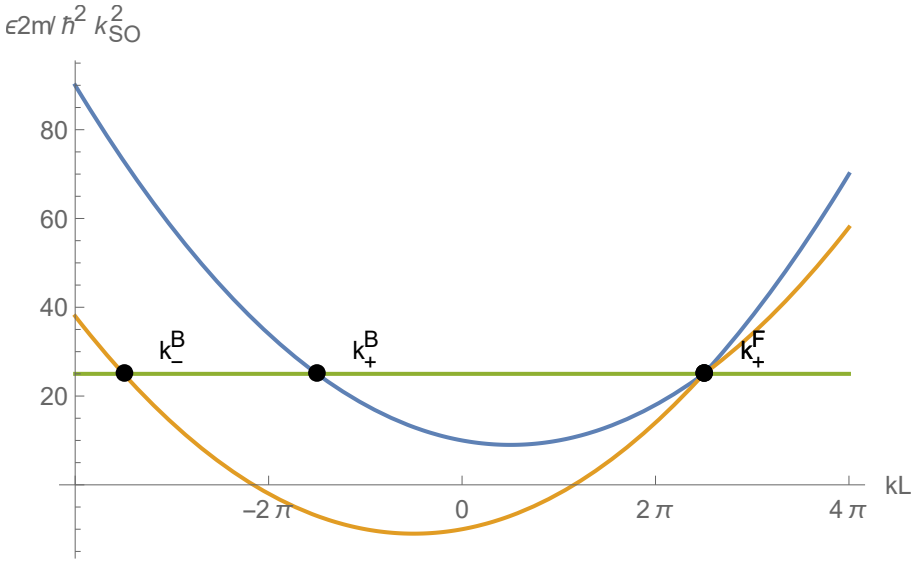

Figure 19: Energy bands for a Zeeman field perpendicular to the wire and strength $\mu B = \frac{\hbar^2 k_{\mathrm{SO}} k_{\mathrm{F}}}{m}$. The energy bands intersect at $k = k_{\mathrm{F}}$.

Figure 19 shows the energy bands for the case where the Zeeman field is perpendicular to the wire. The Fermi level has been chosen so that the energy bands intersect. The same values for k_{SO}, B and k_{F} have been taken for Fig. 20, which shows the spin direction as a function of the wire's direction. The Zeeman field is oriented with the y axis. The figure reveals that when the wire lies along the x axis, the band crossing occurs. Spin states of each band in the degeneracy have opposite directions. For electrons moving forward with momentum k_{+}^{F}, the effective magnetic field created by the Rashba effect cancels with the inplane magnetic field, so the only contribution to the energy comes from the kinetic term.

This effect is very similar to the effect that arises in systems with Rashba SOC and Dresselhaus SOC when the strength of both SOCs is equal. Both energy bands cross for a certain momentum direction because the effective magnetic field vanishes. Unlike the Zeeman term, the Dresselhaus SO (DSO) interaction is a function of k_x and k_y, so the paralelism between both systems is not absolute. For example, for the RSO+DSO case the decoupling is exact along all motion direction. In our case, this only takes place along the direction in which the magnetic field is opposite to the Rashba field. It is clear from Fig. 20 that the maximum distance between Fermi contours happens when the direction of the momentum is opposite to that of the momentum where the contours cross. However, in a system under DSO coupling, this occurs in a direction perpendicular to the contour crossing. [38;39]

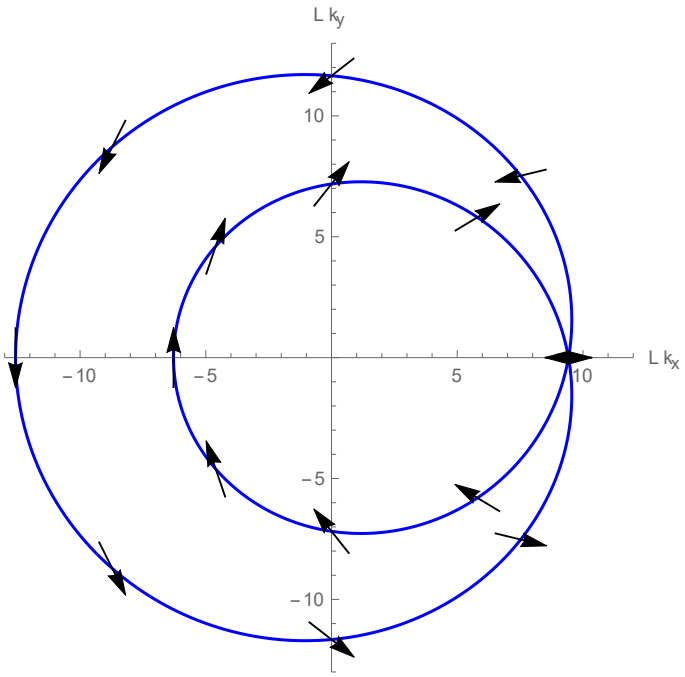

Figure 20: Spin direction as a function of the electron momentum, for each energy band when $\mu B = \frac{\hbar^2 k_{\mathrm{SO}} k_{\mathrm{F}}}{m}$ and $\alpha = \pi/2$. When the wire's direction is perpendicular to the Zeeman field, the two bands with opposite spin intersect.

Since the angles $\theta_{\pm}^{\mathrm{F}}$ are not defined, we can not use the rotation matrix $\hat{\boldsymbol{\mathcal{R}}}$ defined in Sec. (8.2) to express the spatial evolution of the eigenstates with positive momentum. Yet, we know that $|\boldsymbol{v}_{+}^{\mathrm{F}}\rangle$ and $|\boldsymbol{v}_{-}^{\mathrm{F}}\rangle$ are orthogonal, so any spin state can be written as a combination of both of them.

$$\boldsymbol{\Psi}^{\mathrm{F}}(0) = c_{+}|\boldsymbol{v}_{+}^{\mathrm{F}}\rangle + c_{-}|\boldsymbol{v}_{-}^{\mathrm{F}}\rangle \, . \tag{112}$$

The spatial evolution of the state is given by the dynamic phase factor $\mathrm{e}^{\mathrm{i}kr}$

$$\boldsymbol{\Psi}^{\mathrm{F}}(r) = c_{+}\mathrm{e}^{\mathrm{i}k_{+}^{\mathrm{F}}r}|\boldsymbol{v}_{+}^{\mathrm{F}}\rangle + c_{-}\mathrm{e}^{\mathrm{i}k_{-}^{\mathrm{F}}r}|\boldsymbol{v}_{-}^{\mathrm{F}}\rangle = \mathrm{e}^{\mathrm{i}k_{\mathrm{F}}r}\boldsymbol{\Psi}^{\mathrm{F}}(0) \, . \tag{113}$$

We can deduce from Eq. (113) that the rotation matrix will be the identity matrix. This means that any spin state with momentum k_{F} will evolve as a free particle.

9 Simulation of polygons with RSOI and Zeeman field

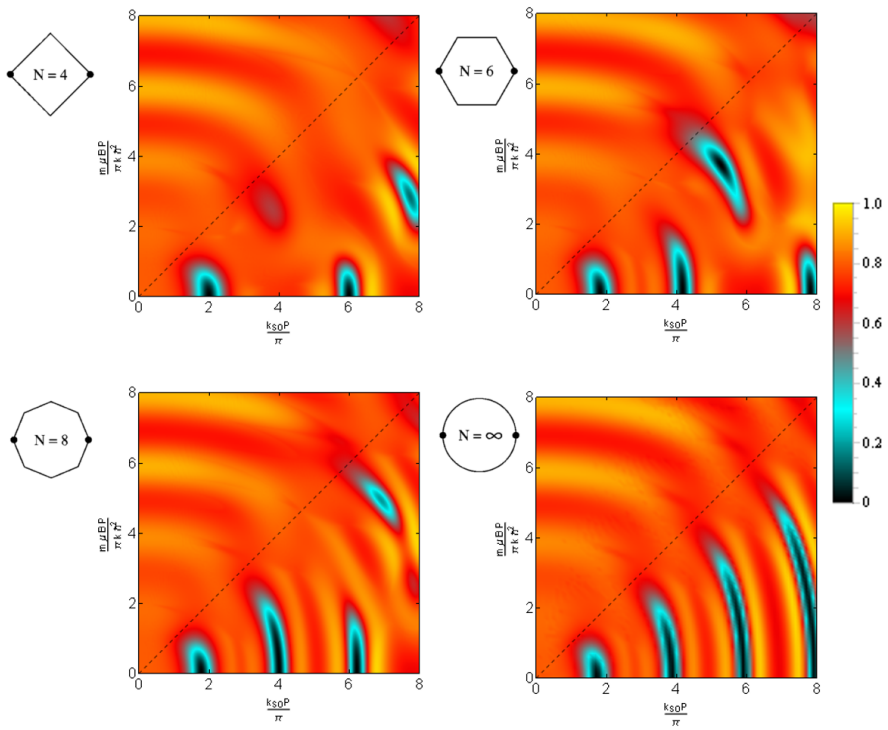

Figure 21: Conductance of different polygons averaged over values of the momentum $k \in [50\pi/\mathrm{P}, 51\pi/\mathrm{P}]$ and input channel, as a function of the dimensionless SO and Zeeman couplings.

The conductance of different polygons averaged over a range of values of k for unpolarized electrons is shown in Fig. 21. The conductance is given in units of $2e^2/h$. The direction of the Zeeman field is $\alpha = 0$, that is to say, it is parallel to the input/output leads. The dimensionless Zeeman coupling is given by $\frac{m\mu BP}{\pi k\hbar^2}$. Spin dynamics under Zeeman coupling depend on the electrons' velocity, opposed to Rashba coupling.[19]

Recalling the results obtained in Fig. 12, for zero Zeeman coupling the conductance displays a series of maxima and minima with a quasiperiod that ranges from $k_{\mathrm{SO}}P = 4\pi$ to 2π as the number of sides increases. Oscillations of period 2π can be identified with the adiabatic limit.[9]

As we explained in Sec. 2.2, the SO cupling is described by an effective radial magnetic field. The magnitude of this effective magnetic field can be deduced by direct comparison between the second and third terms in Eq. (82):

$$\vec{B}_{\mathrm{SO}} = \frac{\hbar k_{\mathrm{SO}}}{m\mu}\vec{p} \times \hat{z} \tag{114}$$

As we increase the in-plane field while maintaining the total magnetic field constant, it can be

seen that the behaviour of the conductance is reversed around the $B_{\mathrm{SO}} = B$ critical line. The position of the maxima and minima are reversed at $B_{\mathrm{SO}} = 0$. This is specially clear in the figure of the ring, where the minima can be found for even values of the SO coupling and no in-plane Zeeman field, while the even values of the dimensionless Zeeman field and no SO coupling correspond to conductance maxima.

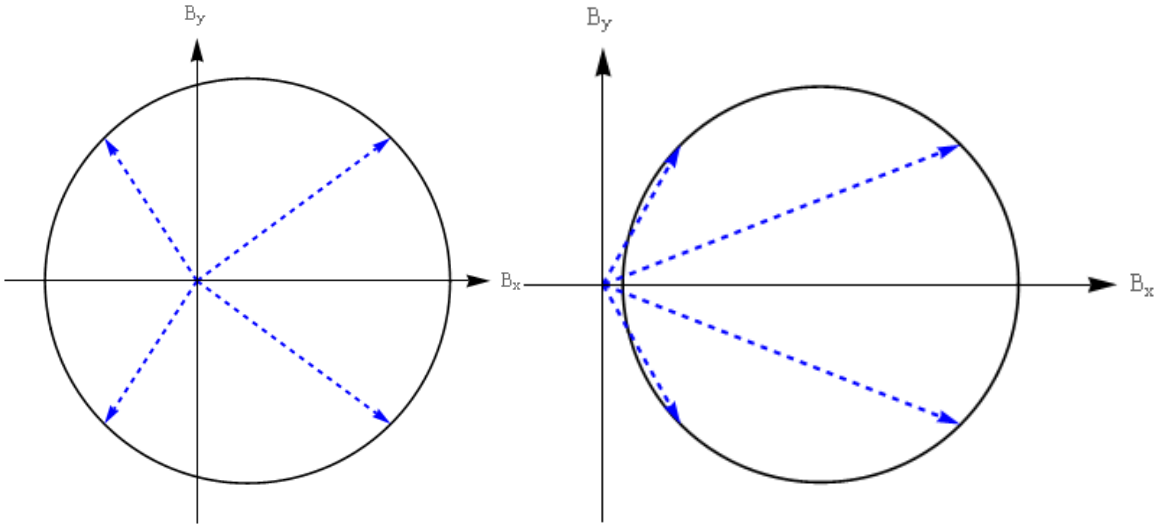

Figure 22: The magnetic field changes the topology at the critical line.

The total magnetic field for the ring is shown in Fig. 22. The Zeeman field has the direction of the positive x-axis. For zero Zeeman field, the total magnetic field has constant modulus, and it is radial to the ring, so it forms a circumference in $\vec{B}$ space. When an in-plane Zeeman field is applied, the circumference is shifted to the right. If the strength of the Zeeman field is less than the SO field ($B < B_{\mathrm{SO}}$), the circumference encircles the origin. In the adiabatic limit, the solid angle corresponding to the Berry phase is $\Omega = 2\pi$ ($\gamma = \pi$). For $B > B_{\mathrm{SO}}$, the circumference does not encircle the origin, so the solid angle is $\Omega = 0$ ($\gamma = 0$).

The behaviour of the conductance is not totally symmetric with respect to the critical line. For example, the conductance of the hexagon has a deep minimum near the critical line, while there is no maximum in the other side of the critical line.

The conductance for small k_{SO} is very much the same for all polygons. Local maxima can be found at even multiples of the dimensionless Zeeman strength, while the minima are located at the odd multiples.

9.1 Dependence of conductance on the direction of Zeeman field

So far we have only studied the dependence of conductance on the strength of the Zeeman field. While the ring has a continuous rotational symmetry, polygons only remain invariant under rotations of an integer multiple of $2\pi/n$, where n is the number of sides of the polygon. In addition, they have

n symmetry planes, as well as inversion symmetry.

The input and output leads break the rotational symmetry of polygons. The only remaining symmetry plane is the horizontal symmetry plane. The vertical plane is not a symmetry plane, since it would interchange the input and output leads. Therefore, the conductance will be the same for angles α and $\alpha' = -\alpha$.

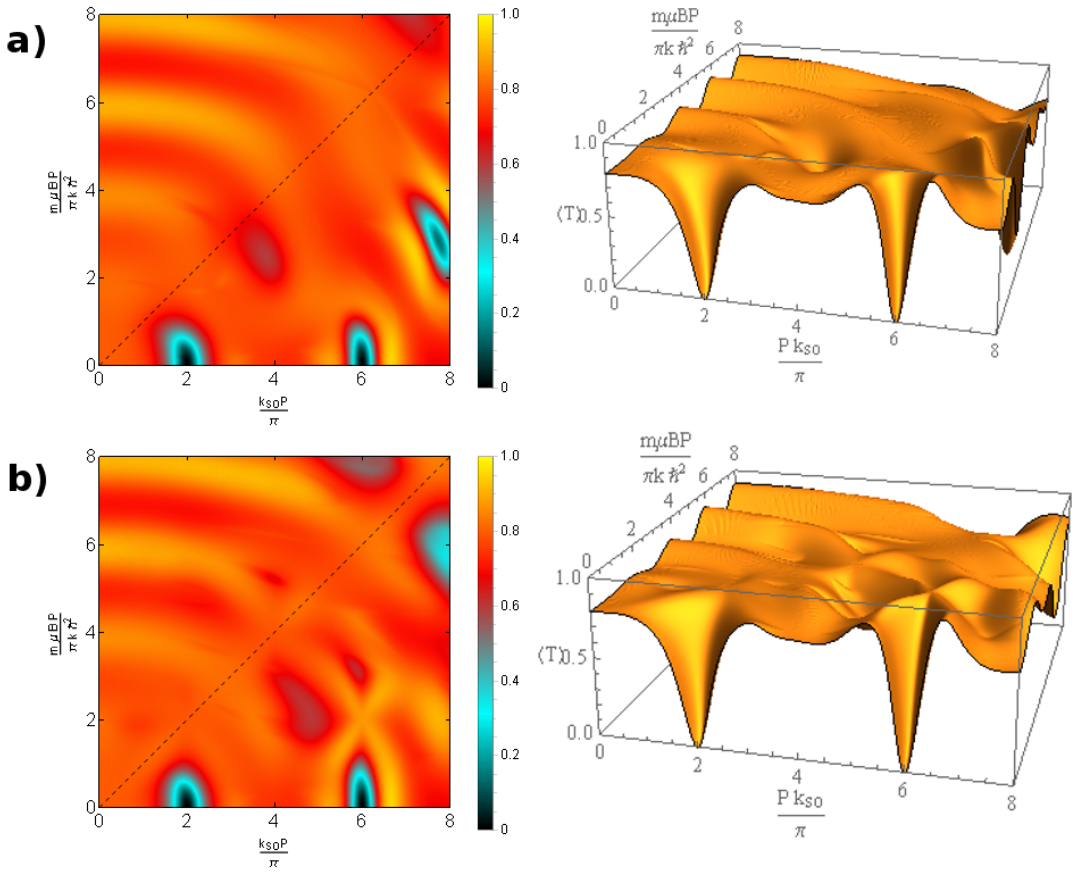

Figure 23: Conductance of a square for a Zeeman field with an orientation of a) $\alpha = 0$ and b) $\alpha = \pi/4$. The dashed line corresponds to the $B_{\mathrm{SO}} = B$ critical line.

We will begin by studying the response of the conductance of a square to the direction of the Zeeman field. Figure 23 presents the conductance for $\alpha = 0$ and $\alpha = \pi/4$. For small values of the Zeeman field strength, the behaviour of both cases is almost identical. For instance, the conductance has two minima near $k_{\mathrm{SO}}P = 2\pi$ and $k_{\mathrm{SO}}P = 6\pi$. The reason for this similar behaviour is that the SO coupling contributes the most to the effective magnetic field.

In the small SO coupling limit, the conductance is also very similar in both cases. For $k_{\mathrm{SO}} = 0$, the Hamiltonian is given by

$$\hat{H} = -\frac{\hbar^2}{2m}\frac{\partial^2}{\partial r^2} + \mu\vec{B}\cdot\vec{\sigma}\,, \tag{115}$$

so the only effect on the spin dynamics is the splitting of the energy bands into two parabolas with opposite spin direction (see Figs. 15 and 16). The magnetic field is constant along the upper and lower paths, so the phase acquired by the electrons moving along both paths is the same. The contribution of the longer paths results in the interference effect that gives rise to the oscillatory effect.

A notable difference between the Figs. 15 and 16 can be found around the critical line, where the conductance for $\alpha = \pi/4$ remains remarkably constant. The conductance for multiple values of α is shown in Fig. 24a. The conductance for low values of k_{SO} is the same for all directions, since it corresponds to the SO and Zeeman free limit. For directions $\alpha = 0$ and $\alpha = \pi/2$, the conductance falls well below 0.7. As we approach the $\alpha = \pi/4$ direction, the oscillations become less pronounced. Moreover, the oscillations show a quasi periodic pattern, with a steadily increasing amplitude.

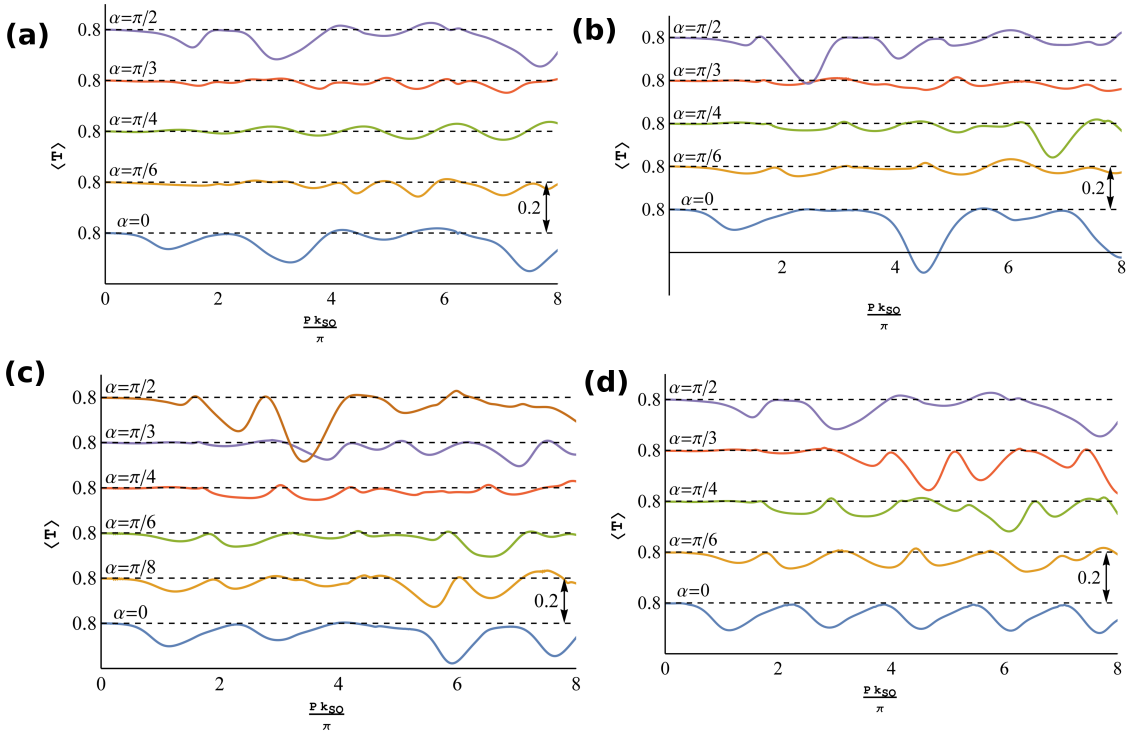

Figure 24: Conductance as a function of the direction of the Zeeman field α along the critical line for a **(a)** square, **(b)** hexagon, **(c)** octagon and **(d)** ring. The plots are shifted vertically for clarity.

As we explained in Sec. 8.6, the energy bands become degenerate when the Zeeman and SO coupling strength are the same, and the Zeeman field is perpendicular to one of the sides of the polygon. The effective magnetic field created by the Rashba effect is perpendicular to the motion of the electron, and in this case, it cancels with the applied Zeeman field. Therefore, electrons with

any spin orientation propagating along this side will not precess, and the interference effect between the upper and lower paths will be mitigated.

The conductance for the hexagon and the octagon along the critical line can be studied in Figs. 24b and 24c respectively.

The Zeeman field is perpendicular to one of the sides of the hexagon when $\alpha = \pi/6$ or $\alpha = \pi/2$. For the octagon, the field is perpendicular for $\alpha = \pi/8$ or $\alpha = 3\pi/8$. As the number of sides of the polygon increases, the length of the sides become smaller, so the side where the spin does not precess has a smaller contribution towards the interference.

When the number of sides of the polygon tends to infinity, there will always be a side that will be perperdicular to the Zeeman field, but its length will be infinitesimal.

9.2 Disordered systems

The polygons studied so far were ballistic (disorder-free) mesoscopic conductors. Disorder stands out among the different factors that can affect the spin evolution. The spin-dependent conductance is obtained from ensemble averages over independent disorder configurations.[40] Disorder can be introduced in several ways. For example, potential disorder along the wires is obtained by randomly located pointlike scatterers. Another kind of disorder is obtained by random fluctuation of the length of the bonds. This kind of disorder is more dangerous for the Rashba-cage effect in quantum networks.[7]

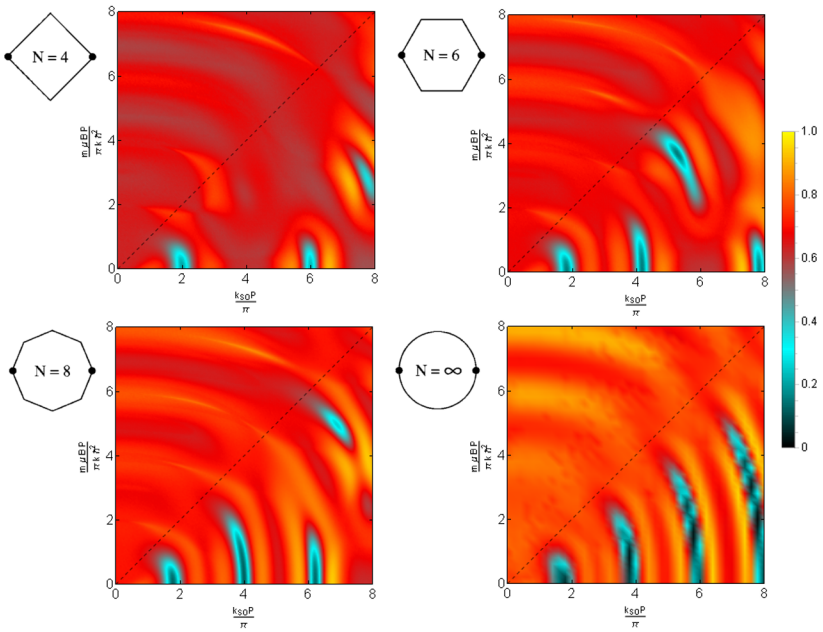

Figure 25: Conductance of different polygons. The conductance has been averaged for polygons with different edge size, keeping the perimeter constant.

The conductance of disordered polygons in Fig. 25 is calculated averaging over disorder configurations for polygons with the same number of edges but different edge size. The conductance has been calculated by taking normally distributed edges, with mean value $l = P/N$, where P is the perimeter and N is the number of edges. The perimeter of all polygons has been kept constant. Comparing the conductance of disordered systems with the one obtained for totally symmetric polygons in Fig. 21, we find that the amplitude of the oscillations has been clearly attenuated. In the Zeeman field free limit, the absolute minima do not reach zero due to the symmetry breaking introduced by disorder. In addition, the value of the conductance of local minima decreases. The periodicity of the spin-orbit will be eventually halved by increasing disorder due to the AAS effect. [36]

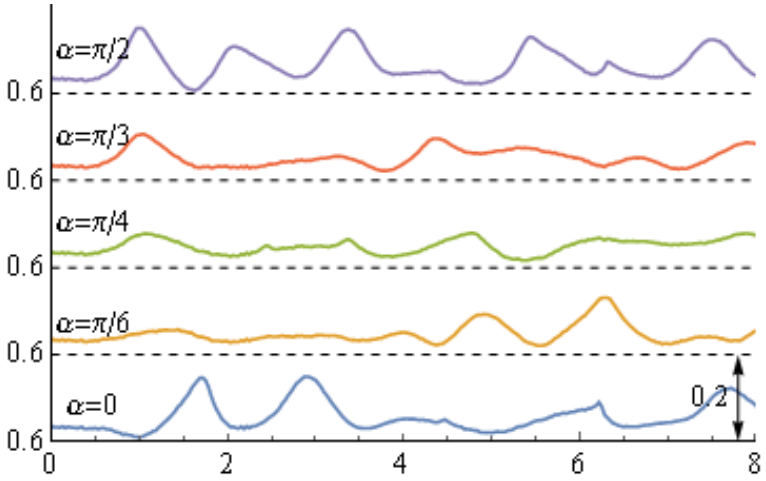

Figure 26: Conductance as a function of the direction of the Zeeman field α along the critical line. The conductance has been averaged for quadrilaterals with different edge size, keeping the perimeter constant.

In the previous subsection we pointed out that for the square, when the direction of the Zeeman field was perpendicular to one of the edges ($\alpha = \pi/4$), the oscillations show a quasi periodic pattern, with a steadily increasing amplitude. This behaviour is suppressed in a disordered system. Another consequence of the introduction of disorder can be appreciated comparing Figs. 24 and 26. The average conductance decreases from 0.8 to nearly 0.6.

10 Conclusions

In this work, we addressed the transport in a 1D mesoscopic ring subject to spin fields. The results for a ring were obtained by studying the transport in a sequence of regular polygons with constant perimeter, by taking the number of edges to infinity. The main results of this work are presented in Chaps. 8 and 9. We generalised the method used in the previous references to study quantum networks pierced by a magnetic flux in the presence of RSO coupling, [7;30;36] to include the presence of an inplane Zeeman field. This method does not rely on perturbation theory, so it is valid for systems with high Zeeman field. In addition, while other methods rely on spin-related phases accumulated by the carriers between input and output leads by following a finite number of channels, this method calculates the exact wavefunction of the electron along the edges.

Specifically, we used this method to study the conductance in different polygons. The obtained results are consistent with the conductance calculated using 2D numerical calculations with the recursive Green's function method and a 1D semiclassical model based on transmission amplitude matrices.[27]

Future works on this subject could include the study of polygons with backscattering junctions. In this work, only ballistic junctions have been considered, but multileg junctions in quasi 1D systems show a strong dependence on the channel width. A connection scheme reflects the presence of an effectively attractive potential at a clean three-leg junction.[41]

References

[1] M. V. Berry, Proc. Roy. Soc. Lond. **A 392** (1984)

[2] Y. Aharonov, D. Bohm, Phys. Rev. Vol. **115** no. 3 (1959)

[3] H. Batelaan and A. Tonomura, Phys. Today **62**(9), 38 (2009)

[4] Y. Aharonov, A. Casher, Phys. Rev. Lett. vol. **53** num. 4 (1984)

[5] D. Bercioux, P. Lucignano, Rep. Prog. Phys. **78**, 106001 (2015)

[6] G. Bihlmayer, Yu.M. Koroteev, P.M. Echenique, E.V. Chulkov, S. Blügel, Surface Science Vol. **600**, Issue 18, Pages 3888-3891 (2006)

[7] D. Bercioux, M. Governale, V. Cataudella, V. M. Ramaglia, Phys. Rev. Lett. vol. **93** num. 5 (2004)

[8] G. Tatara and H. Kohno, Phys. Rev. B **67**,113316 (2003)

[9] D. Frustaglia, K. Richter, Phys. Rev. B **69**, 235310 (2004)

[10] J. Anandan, J. Christian, K. Wanelik, Am. J. Phys. **65** (1997)

[11] S. Pancharatnam, Generalized theory of interference, and its applications, Proceedings of the Indian Academy of Sciences, vol. 44, pp. 247260 (1956).

[12] R. Mignani, Aharonov-Casher effect and geometrical phases, J. Phys. A: Math. Gen. **24**, L421-L423 (1991)

[13] Y. Aharonov, J. Anandan, Phys. Rev. Lett. vol. **58** num. 16 (1987)

[14] M. V. Berry, Physics Today **43**, 34 (1990)

[15] M. König, A. Tschetschetkin, E. M. Hankiewicz, J. Sinova, V. Hock, V. Daumer, M. Schäfer, C. R. Becker, H. Buhmann, L. Molenkamp, Phys. Rev. Lett. **96**, 076804 (2006)

[16] F. Qu, F. Yang, J. Chen, J. Shen, Y. Ding, J. Lu, Y. Song, H. Yang, G. Liu, J. Fan, Y. Li, Z. Ji, C. Yang, L. Lu, Phys. Rev. Lett. **107**, 016802 (2011).

[17] F. Nagasawa, J. Takagi, Y. Kunihashi, M. Kohda, J. Nitta, Phys. Rev. Lett. PRL **108**, 086801 (2012)

[18] B. L. Al'tshuler, A. G. Aronov, B. Z. Spivak, JETP Lett. **33**, 94 (1981)

[19] F. Nagasawa, D. Frustaglia, H. Saarikoski, K. Richter, J. Nitta, Nat. Commun. 4:2526/ncomms3526 (2013)

[20] A. Serio, Quantum graphs: spectrum and magnetic fields, Corso di Laurea Magistrale in Matematica, Università degli Studi di Padova (2014)

[21] M. Baker, X. Faber, Metrized graphs, electrical networks, and fourier analysis (2006)

[22] William Gray Roncal *et al.*, IEEE Global Conference on Signal and Information Processing (2013)

[23] G. Berkolaiko, P. Kuchment R. Carlson, S.A. Fulling, Quantum Graphs and Their Applications, American Mathematical Society (2005)

[24] Sven Gnutzmann & Uzy Smilansky Quantum graphs: Applications to quantum chaos and universal spectral statistics, Advances in Physics, 55:5-6, 527-625 (2006)

[25] S A. Fulling, P. Kuchment, J. H. Wilson, J. Phys. A **40**, 14165-14180 (2007)

[26] D. Bercioux, D. Frustaglia, M. Governale, Phys. Rev. B **72**, 113310 (2005)

[27] H. Saarikoski, J. E. Vázquez-Lozano, J. P. Baltanás, F. Nagasawa, J. Nitta, D. Frustaglia, Phys. Rev. B **91**, 241406 (2015)

[28] S. Viefers, P. Koskinen, P. Singha Deo and M. Manninen, Physica E **21**, (2004)

[29] F. E. Meijer, A. F. Morpurgo, T. M. Klapwijk, Phys. Rev. B **66**, 033107 (2002)

[30] J. Vidal, G. Montambaux, B. Douçot, Phys. Rev. B, vol. **62** num. 24 (2000)

[31] Y. Peleg, R. Pnini, E. Zaarur, Schaum's Easy Oulines Crash Course, Quantum mechanics, Chapter 9, Mc Graw Hill (USA), 2006

[32] W. B. Hodge, S. V. Migirditch, W. C. Kerr, American Journal of Physics **82**, 681 (2014)

[33] C. Wittig, Introduction to Classical and Quantum Relativity, Chapter 3 (2015)

[34] L. D. Landau, E. M. Lifshitz, Mechanics, 3rd ed. (Pergamon Press, Oxford, 1976), pp. 131-132

[35] L. D. Landau, E. M. Lifshitz, Quantum Mechanics: Non-relativistic Theory, 2nd ed. (Pergamon Press, Oxford, England, 1965), pp. 435-437

[36] D. Bercioux, M. Governale, V. Cataudella, V. M. Ramaglia, Phys. Rev. B **72**, 075305 (2005)

[37] J. K. Asbóth, L. Oroszlány, A. Pályi, A Short Course on Topological Insulators, Chapter 10, Springer (2016)

[38] J. Schliemann, J. C. Egues, D. Loss, Phys. Rev. Lett. vol. **90** num. 14 (2003)

[39] J. Schliemann, D. Loss Phys. Rev. B **68**, 165311 (2003)

[40] M. Popp, D. Frustaglia, K. Richter, Phys. Rev. B **68**, 041303(R) (2003)

[41] K. Voo, S. Chen, C. Tang, C. Chu, Phys. Rev. B **73**, 035307 (2006)